IEEE Access
Multidisciplinary ⋮ Rapid Review ⋮ Open Access Journal

Received November 19, 2021, accepted January 3, 2022, date of publication January 6, 2022, date of current version January 20, 2022.

Digital Object Identifier 10.1109/ACCESS.2022.3140977

Understanding Switched-Flux Machines: A MMF-Permeance Model and Magnetic Equivalent Circuit Approach

IMANOL EGUREN[1], GAIZKA ALMANDOZ[1], (Member, IEEE), ARITZ EGEA[1], XABIER BADIOLA[1], AND ANDER URDANGARIN[2]

[1]Goi Eskola Politeknikoa, Mondragon Unibertsitatea, 20500 Arrasate/Mondragón, Spain
[2]ORONA EIC, 20120 Hernani, Spain

Corresponding author: Imanol Eguren (iegurena@mondragon.edu)

The work of Imanol Eguren was supported in part by the Non Doctoral Research Staff Training Programme of the Department of Education of the Basque Government under Grant PRE_2021_2_0240.

ABSTRACT Due to their particular structure, switched-flux permanent magnet machines have become a very interesting alternative for many applications. This is why some recent studies have been focused in the understanding of the operating mechanism of these machines via the MMF-permeance modelling. However, the models that can be found in the literature make some simplifications that reduce their accuracy when predicting the performance of switched-flux machines. For example, the models that can be found in the literature are commonly not precise enough for machines with a wide slot, because the influence of the modulator of the primary side of the machine is neglected. In this article, a precise analytical model is developed for a 6/13 C-Core switched-flux machine via a combination of a magnetic equivalent circuit and a MMF-permeance model. The model is based on the magnetic field modulation principle. The analytical model is used to explain the flux focusing effect and the force generation mechanism of switched-flux machines. A new concept of PM field harmonic efficiency ratio is used to identify the most efficient PM field harmonics of 2 switched-flux machines. The precision of the model is validated via 2D and 3D Finite Element Method simulations, and experimental measurements that were obtained with a linear machine prototype. The results show that the model can predict the performance of switched-flux machines with a high accuracy level.

INDEX TERMS Flux-switching, linear machine, air-gap field modulation, PM brushless machine.

I. INTRODUCTION

Switched-Flux Permanent Magnet Machines (SFPMs) are a kind of Permanent Magnet (PM) machine that has both the armature winding and the PMs mounted in the primary side, while the secondary is composed of a salient ferromagnetic structure. Thanks to their particular structure, these machines combine the high performance of conventional PM machines with the ruggedness of switched-reluctance machines [1]. Moreover, as the PMs and the armature are placed in the same side, the active elements can be easily cooled in SFPMs [1]. These characteristics make them an ideal candidate when high speed or high power density are needed, such as aerospace, automotive or electrical appliance applications [2]–[4].

When talking about linear machines, Linear Switched-Flux Permanent Magnet Machines (LSFPMs) inherit the same advantages of the rotating counterparts. Moreover, conventional PM machines need to place either the armature winding or the PMs along the whole stationary rail. Thanks to their passive ferromagnetic secondary, LSFPMs exhibit a much lower cost when compared to conventional PM machines in long stroke applications [5].

Additional benefits can also be brought by the linear configuration of these machines in many applications. Zhang *et al.* [6] showed that solid-cored LSFPMs could provide an additional safety feature to free-falling vehicles, creating a non-contact braking force and limiting the falling speed. The innate structure of LSFPMs also makes them

The associate editor coordinating the review of this manuscript and approving it for publication was Qinfen Lu.

very suitable for the reciprocating motion of wave energy conversion systems [7] where the complex transmission gearing of rotating machines can be avoided. The high acceleration/deceleration rates that can be achieved by these machines have made them a very interesting alternative for electromagnetic launch systems, where they may replace the conventional steam launch system in the future [8].

A particularly high interest has been generated by LSFPMs in railway transportation. Linear machine driven vehicles can climb higher gradients than conventional systems, thanks to the non-contact thrust generation, moreover, they require less maintenance than conventional systems [9]. Cao *et al*. published a series of papers analysing the complementary and modular LSFPM configuration for railway transportation [10]–[12]. Then, Cao *et al*. [1], compared the performance and the feasibility of a linear induction machine and a LSFPM for Metro line 4 in Guangzhou. The authors concluded that despite the increased initial cost, the difference in cost would be recovered in 493 to 657 days in electrical energy cost savings with the LSFPM.

There is no doubt that switched-flux machines are a very interesting electrical machine technology. However, SFPMs suffer from a severe PM flux leakage in the primary side of the machine. This reduces their PM utilisation, and consequently, the volume of PMs is usually high in these machines [13]. In this aspect, some advanced machine topologies have emerged in the literature, which claim to reduce the PM usage, while the torque capability is enhanced. These are the multi-tooth, E-Core and C-Core machines [14]–[16].

Recently, many studies have analysed the airgap field modulation effect of switched-flux machines [17]–[20]. However, as stated in [19], some papers adopt simplified square-wave permeance and MMF models, and therefore, have a limited precision when predicting the performance of these machines.

A general airgap field modulation theory for electrical machines was published by Cheng *et al*. in [21]. In this work, Cheng *et al*. explain the procedure to analyse many types of electrical machines via the airgap field modulation theory.

The theory has been applied to switched-flux PM machines in [19] and [20]. Wang *et al*. used the airgap field modulation theory to explain the back-EMF generation principle in [19], and the torque generation in [20]. However, in the analytical predictions, the influence of the stator modulator over the amplitude of the airgap field harmonics was considered negligible. This is true in the conventional 12/10 U-Core machine that was analysed in the article. This influence however, depends on the width of the primary slots.

In certain switched-flux machines with a wide slot, like the advanced C-Core topology, the influence of the primary modulator is so high that it changes the order of the dominant airgap field harmonic. Moreover, the flux focusing effect of SFPMs is not contemplated by the model that is introduced in [19] and [20]. The flux focusing effect also depends on the width of the slots. Consequently, the peak values of the airgap flux density that are obtained with the model are far from the values that were obtained by FEM simulations for machines with wide slots.

In this article, a highly precise Magnetic Equivalent Circuit (MEC) and MMF-permeance model is presented for switched-flux machines.

- The model can contemplate the influence of the primary modulator and the flux focusing effect over the spectrum of the airgap flux density.
- The dominant thrust force contributing harmonics of a U-Core and a C-Core machine are identified thanks to the Fourier Series expansion of the permeance model.
- A new concept of PM field harmonic efficiency ratio is introduced. This ratio is used to identify the most efficient PM field harmonics of the U-Core and a C-Core machine, and some suggestions are given for the design of the primary slots of the machines.
- The finite element and experimental results demonstrate the high accuracy of the presented model.

The article is organised as follows. The open-circuit flux-focusing effect is explained via the MEC in section II. Section III analyses the magnetic circuit that is perceived by the coils of the machine. The modulation effect of the magnetic field is described in section IV. The expressions of the flux linkage, back-EMF and thrust force of the machine are derived in section V, and section IV identifies the dominant thrust contributing harmonics, and their interaction. The experimental validation of the results is given in section VII. Finally, the conclusions are given in section VIII.

II. FLUX FOCUSING EFFECT AND OPEN-CIRCUIT AIRGAP FLUX DENSITY

To illustrate the need for a MEC, Fig. 1 shows a comparison between the non-slotted open circuit airgap flux density, the open circuit airgap flux density with only the primary slots, and the totally slotted airgap flux density of a 6/13 C-Core machine. Notice that the variation of the amplitude of the airgap flux density is quite significant in Fig. 1. This variation is driven by the flux-focusing effect of SFPMs. When the machine is slotted, the reluctance of the airgap is increased in the slotted areas. In the slotted machines, the PMs try to introduce the same flux as in the non-slotted machine, so they increase the Magneto-Motive Force (MMF) to compensate the increased reluctance. This increased MMF is responsible of the variation of the amplitude of the airgap flux density in Fig. 1. In the regions that are not slotted, the increased MMF observes the same reluctance as in the non-slotted machine. Therefore, the peak value of the airgap flux density is increased.

It was stated in [19] and [20] that in switched-flux machines in general, the modulator of the primary side does not significantly influence the amplitude of the harmonics of the PM MMF. But in some switched-flux machines with a wide slot, the influence of the primary modulator is so significant, that it changes the order of the dominant airgap MMF harmonic. This section will analyse a 6/13 primary/secondary

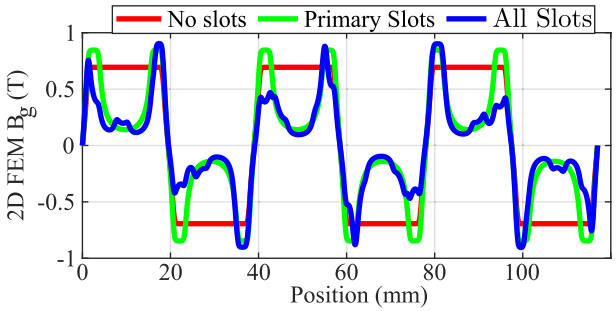

FIGURE 1. Comparison of the non-slotted and the slotted open circuit airgap flux density waveforms.

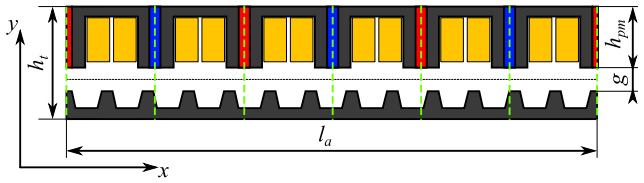

FIGURE 2. General view of the model.

pole C-Core machine in order to illustrate this phenomenon. Fig. 2 shows the linear machine that is modeled in this article, and Table 1 gives the value of its main parameters. The variables from Table 1 are described in Fig. 2 and in Fig. 4.

In this section, a precise MEC model is developed, which is based on the magnetic field modulation theory. Due to the availability of a linear SFPM machine prototype, the model is developed for a linear motor. The model has been developed under the following assumptions:

- The material of the ferromagnetic parts of the machine is an ideal material with an infinite permeability and no saturation.
- The magnetic flux of the airgap is parallel to the y axis of Fig. 2.
- The magnets are assumed to operate inside the linear part of their curve.
- The green dashed lines from Fig. 2 are considered equipotential.
- The end effect is ignored, so that the same results can be obtained with an equivalent rotating machine.
- An axial length of 1 m is assumed when calculating the parameters of the magnetic circuit. In this way, the axial length can be simplified from the expressions.

A. MAGNETIC FLUX DENSITY IN THE AIRGAP—OPEN CIRCUIT

Assuming an ideally periodical machine, the magnetic circuit of the PMs can be simplified to that shown in Fig. 3.

The circuit in Fig. 3 corresponds to a single primary core of a LSFPM. Therefore, an individual circuit must be defined for every single pole of the machine, in order to obtain the flux density distribution of the whole machine. The total airgap flux density is obtained via the concatenation of the airgap flux density of the individual cores.

TABLE 1. Main parameters of the example machine.

Parameter	Symbol	Unit	Value
Active Length	l_a	mm	117
Machine Depth	l_{stk}	mm	35
Total Height	h_t	mm	20
Airgap	g	mm	1
Primary Slot Width	ω_{ps}	mm	11.9
Secondary Slot Width	ω_{ss}	mm	6.2
PM Width	ω_{pm}	mm	2.4
PM Height	h_{pm}	mm	13.7
Turns per Phase	N_{ph}	Turns	200
Supplied Current	I_s	A	1
PM Remanence	B_r	T	1.17
PM Relative Permeability	μ_r		1.06

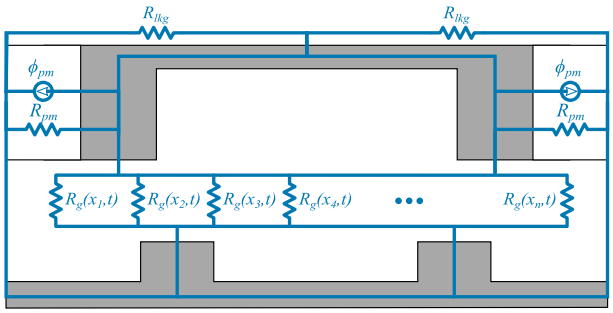

FIGURE 3. Magnetic circuit observed by the magnets.

1) PM EXCITATION

In Fig. 3, ϕ_{pm} is the flux that is generated by a single magnet in the circuit,

$$\phi_{pm} = B_r h_{pm}, \tag{1}$$

R_{pm} is the leakage reluctance of the source,

$$R_{pm} = \frac{\omega_{pm}/2}{h_{pm}\mu_0\mu_r}, \tag{2}$$

and R_{lkg} is the reluctance that is used to account for the flux leakage that appears at the top of the primary of the machine. Its value was approximated assuming a circular path of the leakage flux, with

$$R_{lkg} \approx K_{lkg}\frac{\pi}{8\mu_0} \quad K_{lkg} \approx 1. \tag{3}$$

K_{lkg} is the leakage factor, which is used for the final adjustment of the flux leakage reluctance.

If the airgap is divided into n segments along the x axis, each of the elements that are created will have its own reluctance value, depending on its alignment with the primary and the secondary slots. The calculation of these reluctances is explained below.

2) BASE RELUCTANCE OF THE AIRGAP

This base reluctance refers to the reluctance that would be present in the airgap of the machine if no slots were present. It can be obtained from (4).

$$R_{g_b}(x) = \frac{g(x)}{\mu_0} = \frac{g}{\mu_0} \tag{4}$$

3) EFFECT OF THE PRIMARY AND SECONDARY SIDE MODULATORS

The slotting of the primary and the secondary generates a distortion in the distribution of the airgap flux density. This distortion can be explained via the magnetic field modulation theory [21]. According to the theory, the effect of the N individual modulators of a machine is combined so that the total modulator function, M_t, is

$$M_t(x) = \prod_{i=1}^{N} M_i(x). \tag{5}$$

This means that the effect of each of the individual modulation operators can be obtained individually, and then combined via (5).

The expression for obtaining the waveform of the modulation operators of a switched-flux machine is given in [19]. This modulation operator is calculated via the conformal transformation that was presented by Zhu and Howe in [22]. The expression was introduced for the calculation of the relative permeance of a slotted machine. The concept of relative permeance and the derivation of the expression are explained in detail in [22]. Hence, the readers are advised to refer to this paper in order to understand the origin of the expression.

The drawback of this formula is that it was originally developed by assuming a slot with a finite width and a tooth with an infinite length [22]. Therefore, the effect of the distortion is not estimated perfectly in machines with large slots and narrow teeth. In order to obtain the desired distortion, the modulation operators must be calculated with an enlarged airgap length. Another alternative is to use the improved conformal mapping [23]. In this study, the expressions that have been used are those from [22]. Consequently, an airgap enlarging coefficient, $K_\xi \approx 1$, has been introduced to the formulas in order to adjust the distortion of the modulators.

In this method, a path is defined along the centre of the airgap of the example machine in the complex plane z. The points of the path are defined with their Cartesian coordinates, x and y,

$$z(x, y) = x + j \cdot y. \tag{6}$$

In (6), j is the complex operator.

After defining all the points of the path, these points are transformed to the complex plane w by solving (7) for w

$$z(x, y) = \frac{b_0}{\pi}\left\{\arcsin\left(\frac{w(x, y)}{a}\right) + \frac{K_\xi g}{b_0}\ln\left(\frac{\sqrt{a^2 - w(x, y)^2} + \frac{2K_\xi g}{b_0}w(x, y)}{\sqrt{a^2 - w(x, y)^2} - \frac{2K_\xi g}{b_0}w(x, y)}\right)\right\}, \tag{7}$$

where the value of a is obtained from,

$$a = \sqrt{1 + \left(\frac{2K_\xi g}{b_0}\right)^2}, \tag{8}$$

b_0 is the width of the slot, and g is the length of the airgap.

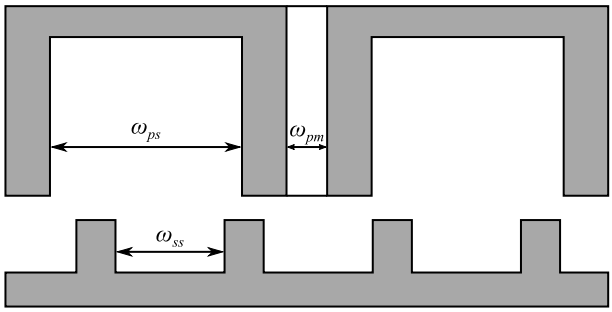

FIGURE 4. Widths of the slots in a switched-flux machine.

After calculating the coordinates of the airgap path in the w plane, the value of the complex modulation operator, $\vec{M}$, can be obtained from

$$\vec{M}(x, y) = \frac{1}{\sqrt{1 + \left(\frac{b_0}{2K_\xi g}\right)^2 - \left(\frac{b_0}{2K_\xi g}w(x, y)\right)^2}}. \tag{9}$$

The value of $\vec{M}$ is a complex number, where the real part indicates the modulation in the y direction of the airgap, and the imaginary value refers to the modulation in the x direction. Hence, the modulation function of the y axis in the center of the airgap, M, is obtained with,

$$M(x) = \mathbb{R}\left\{\vec{M}(x, K_\xi g/2)\right\}. \tag{10}$$

As it can be seen in Fig. 4, there are 3 types of slots in LSFPMs. The primary armature slots, the slots where the PMs are placed, and the slots of the secondary rail. Every single one of these slots has its own modulating effect, which can be obtained by replacing the value of b_0 in (7), (8), and (9) with the corresponding width of each of the slots.

The secondary slots have a particularity. In this case, the secondary rail has been considered the moving part of the machine. Thus, the position of the modulation operator of the secondary rail must be displaced together with the rail in every time step of the calculations.

The modulating function that is obtained with (9) is that of a single slot. Therefore, in order to obtain the total modulation operator of say, the secondary slots, the effect of each individual secondary slot must be obtained first. Then, the total function is obtained from the product of all the single slot modulators. The same goes for the PM and the armature winding slots. Fig. 5 shows the modulation function of the secondary slots of the example machine.

From (5), the total airgap reluctance can finally be obtained with (11)

$$R_g(x, t) = \frac{R_{g_b}(x)}{M_{pa}(x)M_{pm}(x)M_s(x, t)}. \tag{11}$$

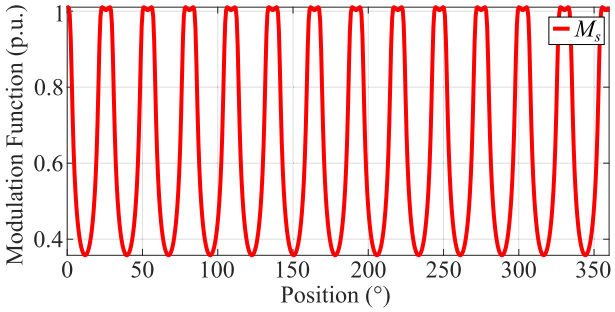

FIGURE 5. Modulation function of the secondary slots.

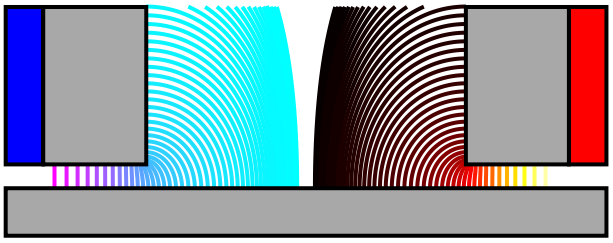

FIGURE 6. Distortion of the magnetic flux lines due to the primary slot modulator in a switched flux machine.

Some might argue that the modulation operator itself is able to predict the flux focusing effect, because it is able to predict the path that the flux lines follow through the airgap. Due to the effect of the slotting, some of the flux lines that are introduced to the airgap are not completely directed in the y axis of Fig. 2. This distortion drives them towards the edges of the teeth. Therefore, the modulation operator can present values that are larger than 1 in some regions, to account for this flux focusing effect. This distortion can be observed in Fig. 6.

However, the distortion of the flux lines through the airgap does not tell the whole story. Notice in Fig. 3 that the reluctances of the airgap are all in parallel, and therefore, they all perceive the same MMF. When there are no slots in the machine, the values of the reluctances of the airgap are uniform through the whole airgap. However, when the slots are placed in the machine, the value of some of those reluctances is increased. The PMs will consequently perceive a higher reluctance in the magnetic circuit. Based on the magnetic flux conservation principle, the MMF that is introduced by the magnets in the circuit will increase to try to compensate this increased reluctance. It is this increase in the MMF that is introduced by the magnets which will create a larger flux density in the airgap regions that are not distorted by the modulation effect. Thus, the MMF that is introduced by the magnets must be recalculated to account for the effect of the slotting.

4) RESOLUTION OF THE MAGNETIC CIRCUIT

For an easier understanding of the magnetic circuit in Fig. 3, a rearranged circuit is given in Fig. 7. Notice that the top and the bottom surfaces in Fig. 7 are at the same potential.

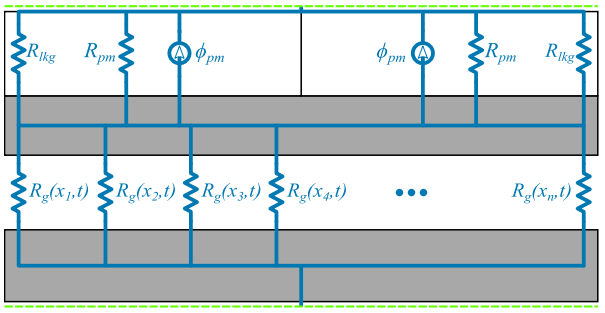

FIGURE 7. Magnetic circuit observed by the magnets, rearranged.

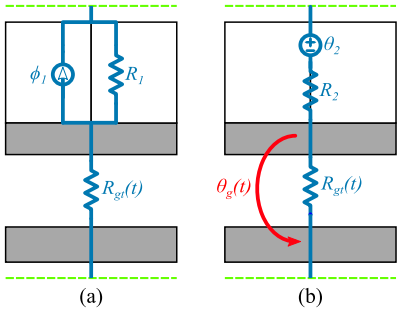

FIGURE 8. Simplification steps of the magnetic circuit that is observed by the magnets. (a) Step 1, simplification of the parallel elements. (b) Step 2, series equivalent circuit.

It is easy to see in Fig. 7 that all the elements in each of the layers of the model are in parallel. Thus, the magnetic circuit can be simplified further to that which is shown in Fig. 8 (a).

The value of ϕ_1 can be obtained with,

$$\phi_1 = 2\phi_{pm}, \tag{12}$$

R_1 is the total leakage reluctance,

$$R_1 = \frac{1}{\frac{1}{R_{lkg}} + \frac{1}{R_{lkg}} + \frac{1}{R_{pm}} + \frac{1}{R_{pm}}}, \tag{13}$$

and the total airgap reluctance is obtained by reciprocating the integral of the airgap permeance.

$$R_{g_t}(t) = \frac{1}{\int_0^{\tau_p} \frac{1}{R_g(x,t)} dx} \tag{14}$$

When analysing electrical or magnetic circuits, an interesting property is the interchangeability of the voltage/MMF sources with current/flux sources. As it can be seen in Fig. 9, the parallel branch of Fig. 8 (a) can be replaced by a series branch with an equivalent MMF source and an equivalent reluctance.

Hence, it can be deduced that the values of the elements in Fig. 8 (b) are

$$\theta_2 = \phi_1 R_1, \text{ and} \tag{15}$$

$$R_2 = R_1, \tag{16}$$

and finally, the total airgap MMF can be obtained with

$$\theta_g(t) = \frac{\theta_2}{R_2 + R_{g_t}(t)} R_{g_t}(t). \tag{17}$$

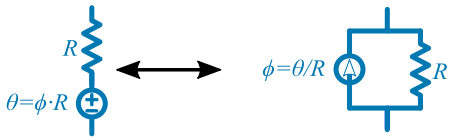

FIGURE 9. Equivalency of the source elements of the magnetic circuit.

The airgap flux density that is generated by the PMs, $B^m_{g_s}$, can be obtained by dividing the total airgap MMF with the spatial distribution of the airgap reluctance

$$B^m_{g_s}(x,t) = \frac{\theta_g(t)}{R_g(x,t)}. \tag{18}$$

However, in the equivalent magnetic circuit, the PM MMF switches abruptly from its maximal value to the minimal value and vice-versa in the centre of the magnets. This abrupt change leads to some spikes in the analytical prediction of $B^m_{g_s}$. In the reality, the PM MMF follows a "s-shaped" curve, as it can be observed in Fig. 1. The shape of the equivalent airgap PM MMF can be rectified by means of a fringing modulator. This modulator is a periodic expression with a period of τ_p. The expression of the function is given in (19), and the waveform of the fringing modulator is given in Fig. 10.

$$M_f(x) = \begin{cases} 1 - e^{-\frac{6x}{\omega_{pm}}} & 0 \le x < \tau_p/2 \\ 1 - e^{-\frac{6(x-\tau_p)}{\omega_{pm}}} & \tau_p/2 \le x < \tau_p \end{cases} \tag{19}$$

After defining the fringing function, it is possible to adjust the reluctance of the airgap with (20).

$$R_{g_f}(x,t) = \frac{R_g(x,t)}{M_f(x)} \tag{20}$$

The waveform of $B^m_{g_f}(x,t)$, which accounts for the fringing, can be obtained by replacing $R_g(x,t)$ in (14), (17) and (18) with (20).

5) ANALYSIS OF THE FLUX FOCUSING EFFECT

In this section, the results that have been obtained for the example machine from the magnetic equivalent circuit are validated via 2D Finite Element Method (FEM) simulations. Despite the simplifications, the waveforms of the airgap flux density that were obtained from the 2D FEM simulation and the MEC are very close to each other. This happens because the magnetic materials of the machine do not suffer a heavy saturation in the open circuit condition.

The different stages of the modulation process are now individually analysed to demonstrate the importance of the primary modulator in the operation of wide slot opening SFPMs. Notice that when displaying the spectrum of the different waveforms, only the amplitude of the positive order harmonics is given, in order to obtain a more visually pleasant figure.

First of all, the result of the virtual machine with no slots can be obtained from the MEC by defining

$$R_{g_f}(x) = \frac{R_{g_b}(x)}{M_f(x)\,M_{pm}(x)}. \tag{21}$$

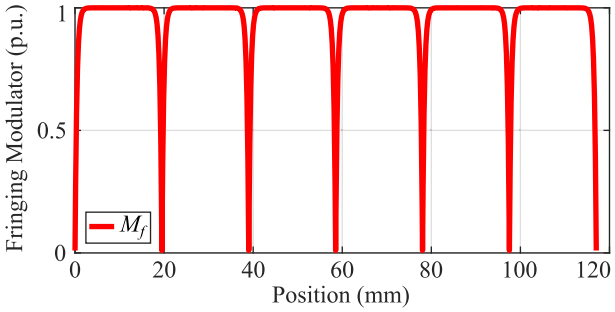

FIGURE 10. Waveform of the fringing modulator.

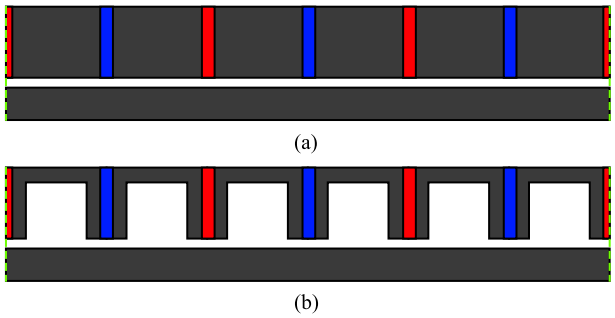

FIGURE 11. Simulation models. (a) Virtual machine with "no slots." (b) Virtual machine with all the primary slots.

Notice in Fig. 11 (a) that the modulation effect of the magnets is introduced when the PMs are introduced in the machine. Therefore, the airgap flux density of the virtual "non-slotted" machine actually contains the PM slots.

The waveform of the open circuit airgap flux density is given in Fig. 12 (a). The spectrum in Fig. 12 shows a clear dominance of the fundamental harmonic of the PM field, of order $p_{pm} = 3$.

Then, the airgap flux density for the machine with all the primary slots (Fig. 11 (b)) is obtained with

$$R_{g_f}(x) = \frac{R_{g_b}(x)}{M_f(x)\,M_{pm}(x)\,M_{ps}(x)}. \tag{22}$$

The open circuit airgap flux density of this second case is given in Fig. 13. This time, the distorting effect of the primary modulator is so significant, that the dominant harmonic is changed. The largest amplitude harmonic can be found to be the $3p_{pm} = 9$ in Fig. 13 (b). Hence, qualifying this distorting effect as negligible would be incorrect. This effect is a crucial part in the operation of large slot-opening SFPMs.

Finally, the waveform of the airgap flux density that is produced by the magnets in the totally slotted machine from Fig. 2 is given in Fig. 14, and can be obtained from

$$R_{g_f}(x,t) = \frac{R_{g_b}(x)}{M_f(x)\,M_{pm}(x)\,M_{ps}(x)\,M_s(x,t)}. \tag{23}$$

Notice that the primary slots do not crate any additional harmonic components in Fig. 12 and Fig. 13. They only modify the amplitude of the existing harmonics, due to the flux focusing effect. This happens because the period of the

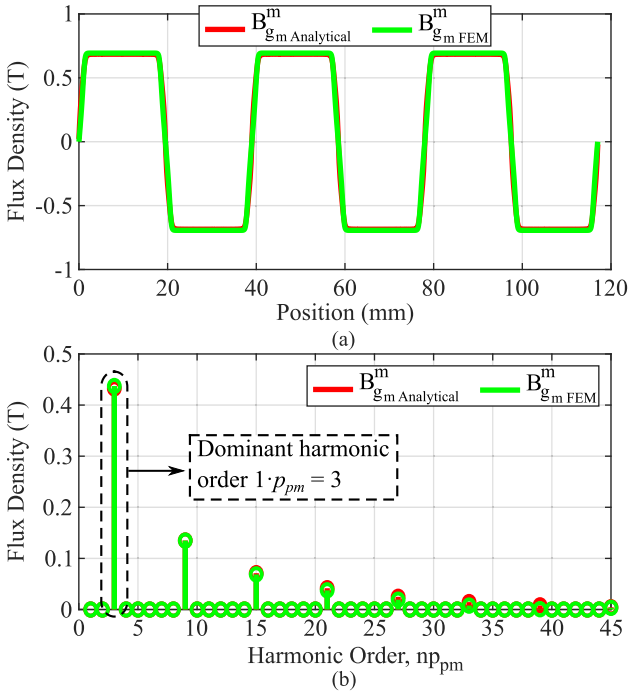

FIGURE 12. Open circuit airgap flux density of the machine with "no slots." (a) Waveform, and (b) spectrum.

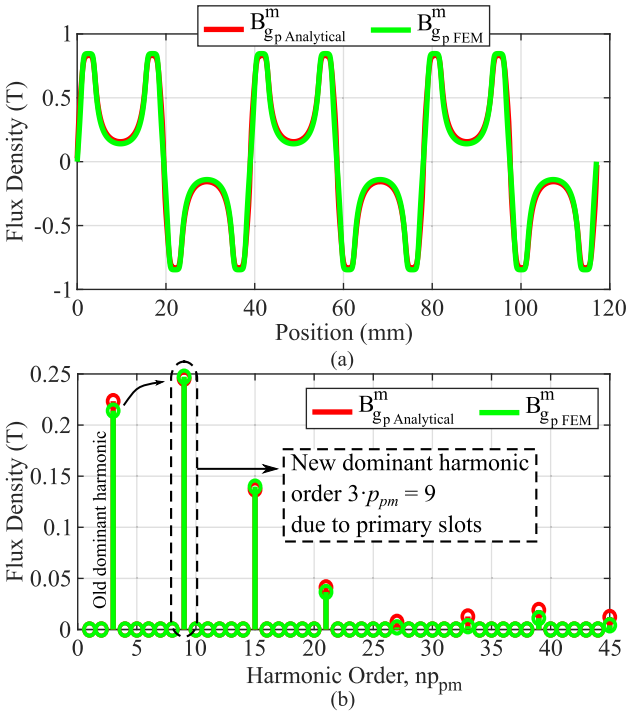

FIGURE 13. Open circuit airgap flux density of the machine with all the primary slots. (a) Waveform, and (b) spectrum.

PM field wave is a multiple of the period of the primary modulator functions. On the other hand, when the secondary modulator is introduced in the machine, a handful of new harmonics emerge in Fig. 14. Table 2 shows a comparison of the amplitude of the main airgap flux density harmonics in all the three cases. An amplitude of ≈ 0 is showed in the table for the harmonics which have an amplitude of $<10^{-5}$. This amplitude can be attributed to the numerical error.

The periods of the modulator of the secondary and the PM field are not multiples. Hence, the new harmonics emerge from the interference of the magnetic field that is produced by the primary and the secondary modulator function. The modulation phenomenon that creates these additional harmonics is analysed in detail in section V.

III. ARMATURE AIRGAP FLUX DENSITY

In order to obtain a proper representation of the armature airgap flux density, the winding function and the turns function must be defined first. In this case, the analysis starts with the definition of the star of slots.

A. WINDING FUNCTION AND TURNS FUNCTION

1) STAR OF SLOTS

The star of slots is a very useful tool when defining the distribution of the conductors of a phase. It is a vectorial representation of the fundamental component of the back-EMF that is going to be induced in each of the slots. The definition of the star of slots is slightly different in switched-flux machines when compared to that of conventional PM machines.

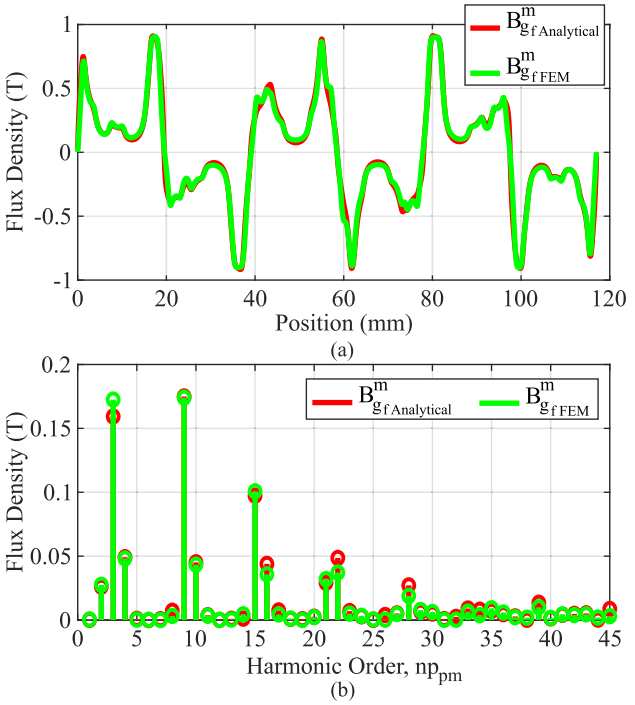

FIGURE 14. Comparison of the airgap flux density produced by the magnets, analytical tool with fringing function vs. FEM. (a) Waveform, and (b) spectrum.

The procedure starts with the definition of the number of pole-pairs of the armature winding, p_w [24]

$$p_w = n_s - p_{pm}. \tag{24}$$

TABLE 2. Amplitude of the airgap flux density harmonics.

Harmonic Order	Non-Slotted		Primary Slots		All Slots	
	Analytical	FEM	Analytical	FEM	Analytical	FEM
2	≈ 0	≈ 0	≈ 0	≈ 0	0.03	0.03
3	0.43	0.44	0.22	0.21	0.16	0.17
4	≈ 0	≈ 0	≈ 0	≈ 0	0.05	0.05
9	0.13	0.13	0.25	0.25	0.17	0.17
10	≈ 0	≈ 0	≈ 0	≈ 0	0.05	0.04
15	0.07	0.07	0.14	0.14	0.10	0.10
16	≈ 0	≈ 0	≈ 0	≈ 0	0.04	0.03
22	≈ 0	≈ 0	≈ 0	≈ 0	0.05	0.04
28	≈ 0	≈ 0	≈ 0	≈ 0	0.03	0.02

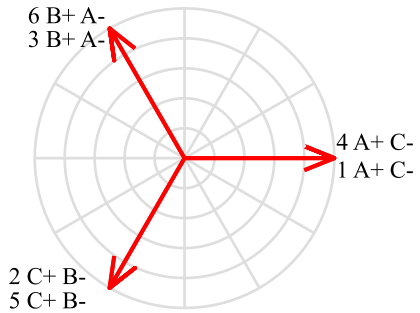

FIGURE 15. Star of slots of the 6/13 C-Core machine.

n_s and p_{pm} are the number of secondary teeth and the PM pole-pair number.

The periodicity of the winding, t_p, in switched-flux machines is [25]

$$t_p = \gcd\left(n_p \frac{n_l}{2}, p_w\right). \tag{25}$$

n_p is the number of primary poles, and n_l is the number of layers of the winding, so that $n_l = 1$ for single layer machines, and $n_l = 2$ four double layer machines.

The spokes-per-phase, q_{ph}, are given by

$$q_{ph} = \frac{n_p n_l}{2 t_p m}, \tag{26}$$

where m is the number of phases of the machine, and the electrical displacement between adjacent primary slots, α_e is expressed as

$$\alpha_e = p_w \frac{2\pi}{n_p}. \tag{27}$$

The star of slots of the example machine was obtained based on the preceding equations. The result is shown in Fig. 15. The machine has a winding periodicity value of 2, that is why there are only 3 vectors to represent the 6 slots of the machine.

2) CONDUCTOR DISTRIBUTION

Once the star of slots is defined, the conductor distribution function, $C(x)$ can be obtained. This starts with the analysis of a single coil of the machine. The shape of the conductor distribution function will change according to the layout of the conductors of the coil inside the slot. In the example machine, with $t_p = 2$ and $q_{ph} = 1$, and a uniform distribution of the turns inside the slot, the shape of the conductor distribution function is shown in Fig. 16.

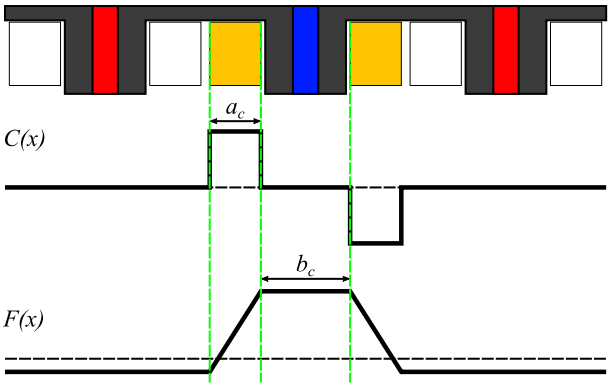

FIGURE 16. Waveforms of the conductor distribution function and the winding function in a single periodicity of the example machine.

Assuming a periodic coil with Z turns, a width of a_c and a coil span of b_c, its conductor distribution C_c function can be defined as

$$C_c(x) = \begin{cases} 0 & \frac{-n_p\tau_p}{2t_p} \le x < \frac{-b_c}{2} - a_c \\ \frac{Z}{a_c} & \frac{-b_c}{2} - a_c \le x < \frac{-b_c}{2} \\ 0 & \frac{-b_c}{2} \le x < \frac{b_c}{2} \\ \frac{Z}{a_c} & \frac{b_c}{2} \le x < \frac{b_c}{2} + a_c \\ 0 & \frac{b_c}{2} + a_c \le x < \frac{n_p\tau_p}{2t_p}. \end{cases} \tag{28}$$

At this point, the winding function of that coil can be obtained by integration of the conductor distribution function,

$$F_c(x) = \int C(x)dx. \tag{29}$$

The winding function of a phase, F_{ph}, is the sum of the individual winding functions of the coils of a phase that are inside of a winding periodicity,

$$F_{ph}(x) = \sum_{i=1}^{n_c} F_{c_i}(x). \tag{30}$$

n_c is the number of coils of a phase inside a winding periodicity.

In conventional machines, the shape of the winding function and the per-current-unit airgap MMF $F_g(x)$ is the same [26].

However, due to the discontinuous path in the magnetic circuit of the coils in PM switched-flux machines, the shape of the airgap MMF is different to that of $F(x)$. This happens because the slots of the PMs act as additional airgaps that the flux lines of the coil have to cross before returning to the origin. Therefore, most of the field of an armature coil is concentrated in the two core-pieces that it is wound at. In order to contemplate this phenomenon, the magnetic circuit of a coil is defined in Fig. 18.

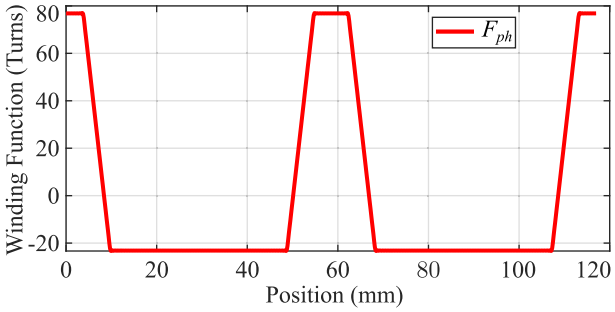

FIGURE 17. Winding function of the example machine.

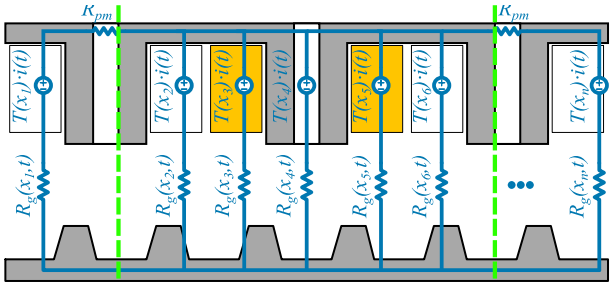

FIGURE 18. Magnetic circuit of a coil in the example machine.

Notice that the MMF sources of the circuit in Fig. 18 are modelled with the turns function. This function is nothing but the winding function with a bias. The function describes the spatial distribution of the physical amount of turns of a winding. Hence, for example, if a tooth is left unwound, the value of the turns function along that tooth will be 0, whereas the winding function could still have a non-zero value. The bias of the turns function for the example machine, T_0, is given by

$$T_0 = t_p Z \frac{a_c + b_c}{n_p \tau_p}. \tag{31}$$

B. MAGNETIC CIRCUIT OF THE COILS

Notice that there is an increased reluctance in the circuit for the flux lines that pass through the permanent magnets in the edges of Fig. 18. This increased reluctance acts as an enlarged airgap, and therefore, it influences the distribution of the flux that is generated by the coil. Fig. 19 shows the spatial distribution of the increased airgap length. The flux lines that pass through the last half-core must cross the permanent magnets. Therefore, the width of the magnetic circuit changes from $\tau_p/2 - \omega_{pm}/2$, to h_{pm}. Consequently, the value of the airgap-increasing reluctance, $R_{pm_x}(x)$ must be normalised to account for this change. The readers might also notice that there is another PM in the centre of Fig. 18. However, the influence of this magnet is so small, that the reluctance can be neglected for simplicity of the circuit.

If the airgap reluctance of a coil is defined as

$$R_{gc}(x,t) = R_g(x,t) + R_{pm_x}(x), \tag{32}$$

the magnetic circuit of a coil can be simplified to that shown in Fig. 20 (a). By using the equivalency that was shown in Fig. 9, the magnetic circuit can be transformed into a series of parallel flux sources and resistors Fig. 20 (b). Then, the total resistance of the coil's circuit and the equivalent total flux (Fig. 20 (c)) can be obtained with

$$R_{gc_t}(t) = \frac{1}{\int_{\frac{-n_p\tau_p}{2t_p}}^{\frac{n_p\tau_p}{2t_p}} \frac{1}{\frac{1}{R_{gc}(x,t)}} dx}, \text{ and} \tag{33}$$

$$\phi_{c2}(t) = \int_{\frac{-n_p\tau_p}{2t_p}}^{\frac{n_p\tau_p}{2t_p}} \phi_{c1}(x,t)\, dx. \tag{34}$$

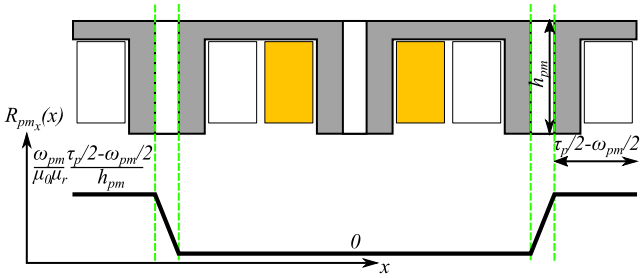

FIGURE 19. Reluctance increase in the magnetic circuit of a coil.

Finally, the per current-unit MMF can be obtained from (35), by assuming that $i(t) = 1$,

$$F_g(x,t) = \frac{T(x)\, i(t) - \theta_{cg_t}(t)}{R_{gc}(x,t)} R_g(x,t), \tag{35}$$

and therefore, the airgap flux density of coil c, $B^a_{g_c}(x,t)$ is

$$B^a_{g_c}(x,t) = \frac{F_g(x,t)\, i(t)}{R_g(x,t)}. \tag{36}$$

The total expressions for the turns function and airgap flux density of a phase, $T_{ph}(x)$ and $B^a_{g_{ph}}(x,t)$ respectively, are the sum of those of the individual coils of that phase.

$$T_{ph}(x) = \sum_{n=1}^{n_c} T_n(x) \tag{37}$$

$$B^a_{g_{ph}}(x,t) = \sum_{n=1}^{n_c} B^a_{g_{c_n}}(x,t) \tag{38}$$

The total flux density that is generated by the armature, $B^a_g(x,t)$, which is shown in Fig. 21 (b), is obtained with the sum of the individual $B^a_{g_{ph}}(x,t)$ of each of the phases.

$$B^a_g(x,t) = \sum_{k=1}^{m} B^a_{g_{ph}}(x,t) \tag{39}$$

IV. MODULATION OF THE MAGNETIC FIELD

In this section, the harmonics of the open circuit airgap flux density and the armature airgap flux density are analysed via the magnetic field modulation principle.

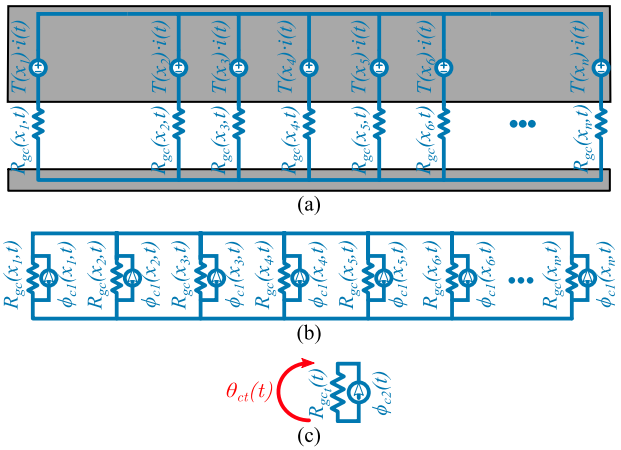

FIGURE 20. Simplification of the magnetic circuit of a coil.

A. OPEN CIRCUIT AIRGAP FIELD HARMONICS

The analysis procedure starts with the obtention of the airgap flux density that is generated by the PMs in the slotted machine, B_{gs}^{m}. According to [19] the total modulating function is the product of the individual modulator functions. Therefore, the modulated B_{gs}^{m} can be obtained with

$$B_{gs}^{m}(x,t) = B_{g}^{m}(x)\, M_{p}(x)\, M_{s}(x,t)\,. \tag{40}$$

B_{g}^{m} is the flux density that is introduced by the PMs in the airgap of a virtual machine with no slots, but, accounting for the flux-focusing effect that was explained in section II. Fig. 22 shows a graphical comparison between B_{g}^{m} and the real airgap flux density in a machine without slots. To obtain this function, the airgap flux density that was calculated for the slotted machine must be divided with the modulators of the secondary rail, the PM slots and the armature slots.

$$B_{g}^{m} = \frac{B_{gs}^{m}(x,t)}{M_{s}(x,t)\, M_{pm}(x)\, M_{pa}(x)} \tag{41}$$

Remember that there are two different types of slots in the primary of switched-flux PM machines. These are the slots of the PMs and the slots where the armature coils are introduced. M_p is the function that describes the combined effect of both of these slots,

$$M_{p}(x) = M_{pa}(x)\, M_{pm}(x)\,, \tag{42}$$

where $M_{pa}(x)$ is the modulating function of the armature coil slots, and $M_{pm}(x)$ is the modulation function of the PM slots.

As it can be seen in Fig. 23 the modulating functions are periodic functions with an average value. Therefore, they can be expressed as a fourier series as in (43) and (44).

$$M_{p}(x) = M_{p0} + \sum_{i=-\infty}^{\infty} \vec{M}_{p_i} e^{jn_p i\left(\gamma - x\frac{2\pi}{n_p \tau_p}\right)} \tag{43}$$

$$M_{s}(x,t) = M_{s0} + \sum_{v=-\infty}^{\infty} \vec{M}_{s_v} e^{jn_s v\left(\xi - x\frac{2\pi}{n_p \tau_p} - V\frac{2\pi}{n_p \tau_p}t\right)} \tag{44}$$

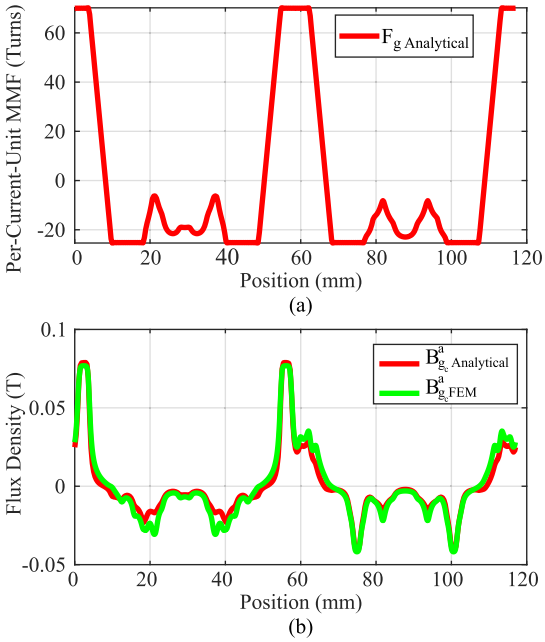

FIGURE 21. Per-current-unit airgap MMF (a) and airgap flux density (b) generated by a periodic coil.

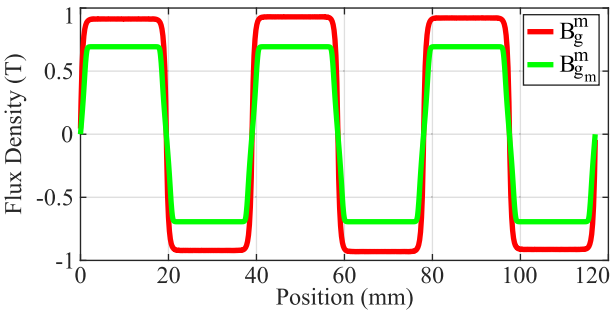

FIGURE 22. Airgap flux density of a virtual machine with no slots, B_{gm}^{m}, and equivalent non-slotted airgap flux density accounting for the flux-focusing effect, B_{g}^{m}.

M_{p0} and M_{s0} are the average values of the primary and secondary modulation functions. $\vec{M}_{p_i}$ and $\vec{M}_{p_v}$ are the vectors of the i-th and v-th harmonics. n_p and n_s are the number of armature slots in the primary and the number of secondary slots. τ_p is the primary pole pitch, and γ and ξ are the initial phases of the functions in radians. Notice in (44) that the positive sense of the speed, V, translates the secondary rail to the left side of Fig. 2.

On the other hand the equivalent non-slotted airgap flux density, B_{g}^{m} is also a periodic function. In this case, as shown in Fig. 22, there is no average value, and the function can be expressed as

$$B_{g}^{m}(x) = \sum_{h=-\infty}^{\infty} \vec{B}_{gh}^{m} e^{jhp_{pm}\left(\varphi - x\frac{2\pi}{n_p \tau_p}\right)}. \tag{45}$$

$\vec{B}_{gh}^{m}$ is the vector of the h-th harmonic, p_{pm} is the number of PM pole pairs, and φ is the initial phase of the PM field.

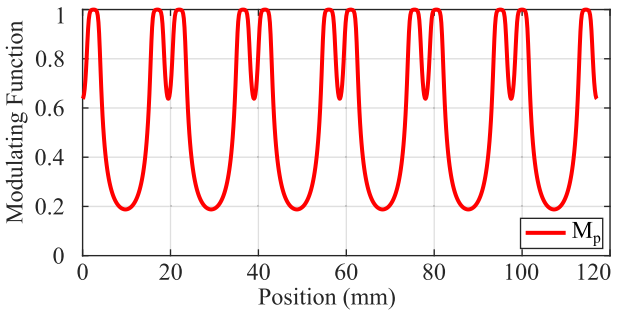

FIGURE 23. Modulation function of the primary slots of the example machine.

Notice that the period of M_p is half of that of B_g^m. Therefore, the combination of these functions, B_{gp}^m, does not create any additional harmonics, and can also be expressed as a Fourier series,

$$B_{g_p}^m(x) = \sum_{n=-\infty}^{\infty} \vec{B_{gp_n}^m} e^{jnp_{pm}\left(\varphi - x\frac{2\pi}{np\tau_p}\right)}, \tag{46}$$

where $\vec{B_{gp_n}^m}$ is the vector of the n-th harmonic.

Now, the modulated airgap flux density that is produced by the magnets can be deduced to be

$$B_{g_s}^m(x,t) = B_{g_p}^m(x) M_s(x,t), \tag{47}$$

which yields

$$\begin{aligned} B_{g_s}^m(x,t) = M_{s0} &\sum_{n=-\infty}^{\infty} \vec{B_{gp_n}^m} e^{j\left(np_{pm}\varphi - np_{pm}x\frac{2\pi}{np\tau_p}\right)} \\ &+ \sum_{n=-\infty}^{\infty}\sum_{v=-\infty}^{\infty} \vec{M_{s_v}} \vec{B_{gp_n}^m} \\ &\times e^{j\left(np_{pm}\varphi + vn_s\xi - x\frac{2\pi}{np\tau_p}(np_{pm}+vn_s) - vn_sV\frac{2\pi}{np\tau_p}t\right)}. \end{aligned} \tag{48}$$

Notice that the first term of (48) is not time-dependant. Therefore, its harmonic content stays at the same position no matter the position of the secondary rail. On the other hand, the second term is indeed time-dependant, and the harmonics that are described there will vary their position when the secondary rail is displaced.

Also notice that the number of pole pairs of the static term is the same as that of the non-modulated B_g^m, whereas the pole pair number of the dynamic harmonics is the result of the interference between the original B_g^m harmonics and the harmonics of the secondary modulator.

B. THE MODULATED ARMATURE MMF

In order to explain the interaction of the harmonics of the armature MMF with those of the PM field, the Fourier analysis is applied to the armature MMF in this section. To start with, notice that the armature MMF from Fig. 21 (a) does not have the same period as the winding function in Fig. 17. There are some subharmonics that emerge because of the discontinuous path of the magnetic circuit in the primary of the machine. These subharmonics do not contribute to the PM force, and hence, they are neglected in this section. Fig. 24 shows the initial and the simplified per-current-unit MMF waveforms and their spectra, where the neglected subharmonics are highlighted in green.

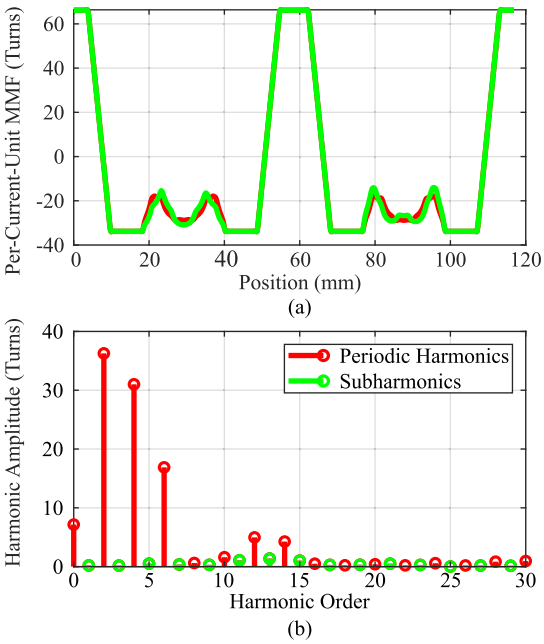

FIGURE 24. Simplification of the per-current-unit airgap MMF. (a) Waveform and (b) spectrum.

Much like in the case of the PM field, the period of the airgap MMF that is produced by the armature and that of the primary modulator are multiples of each other. Hence, no additional harmonic is produced due to their interaction. Therefore, it is possible to define the combination of the per-current-unit airgap MMF of a phase and the primary modulator, $F_{gp_{ph}}(x,t)$ as a Fourier series as

$$F_{gp_{ph}}(x,t) = \sum_{k=-\infty}^{\infty} \vec{F_{gp_k}} e^{jkt_p\left(\delta - x\frac{2\pi}{np\tau_p}\right)}. \tag{49}$$

$\vec{F_{gp_k}}$ is the vector of the k$^{\text{th}}$ harmonic and δ is the initial phase of the waveform in radians. The MMF of that phase will therefore be obtained by multiplying $F_{gp_{ph}}(x,t)$ with the supply current,

$$i_{ph}(t) = \hat{I}\cos(\omega t + \phi), \tag{50}$$

which is assumed to be a perfect cosine with no harmonic content, and can be represented exponentially as

$$i_{ph}(t) = \frac{\hat{I}}{2}e^{j(\omega t+\phi)} + \frac{\hat{I}}{2}e^{-j(\omega t+\phi)}. \tag{51}$$

$\hat{I}$ is the peak value of the current, ω is the angular velocity of the current vector, and ϕ is its initial angle. Therefore, the

airgap MMF of a phase, $MMF_{gp_{ph}}(x,t)$ yields

$$\begin{aligned} &MMF_{gp_{ph}}(x,t) \\ &= \frac{\hat{I}}{2}\sum_{k=-\infty}^{\infty} \vec{F_{gp_k}} e^{j\left(kt_p\delta - kt_p x\frac{2\pi}{n_p\tau_p}+\omega t+\phi\right)} \\ &\quad + \frac{\hat{I}}{2}\sum_{k=-\infty}^{\infty} \vec{F_{gp_k}} e^{j\left(kt_p\delta - kt_p x\frac{2\pi}{n_p\tau_p}-\omega t-\phi\right)}. \end{aligned} \tag{52}$$

Assuming a perfectly balanced and symmetrical three phase 6/13 pole switched-flux machine,

$$kt_p\delta_a = kt_p\delta,\ kt_p\delta_b = kt_p\left(\delta+\tfrac{2\pi}{3t_p}\right),\ kt_p\delta_c = kt_p\left(\delta-\tfrac{2\pi}{3t_p}\right) \tag{53}$$

and,

$$\phi_a = \phi \quad \phi_b = \phi - \frac{2\pi}{3} \quad \phi_c = \phi + \frac{2\pi}{3}, \tag{54}$$

the total 3 phase armature MMF can be deduced to be

$$\begin{aligned} &MMF_{gp}(x,t) \\ &= MMF_{gp_a}(x,t) + MMF_{gp_b}(x,t) + MMF_{gp_c}(x,t) \\ &= \frac{\hat{I}}{2}\sum_{k=-\infty}^{\infty} \vec{F_{gp_k}} e^{j\left(kt_p\delta - kt_p x\frac{2\pi}{n_p\tau_p}+\omega t+\phi\right)} \\ &\quad \times\left(1+2\cos\left(\frac{2\pi}{3}(k-1)\right)\right) \\ &\quad + \frac{\hat{I}}{2}\sum_{k=-\infty}^{\infty} \vec{F_{gp_k}} e^{j\left(kt_p\delta - kt_p x\frac{2\pi}{n_p\tau_p}-\omega t-\phi\right)} \\ &\quad \times\left(1+2\cos\left(\frac{2\pi}{3}(k+1)\right)\right). \end{aligned} \tag{55}$$

The modulated airgap MMF, $MMF_M(x,t)$ can now be obtained with

$$MMF_M(x,t) = MMF_{gp}(x,t)\,M_s(x,t). \tag{56}$$

From (44), (55), and (56), it can be deduced that

$$\begin{aligned} &MMF_M(x,t) \\ &= M_{s0}\frac{\hat{I}}{2}\sum_{k=-\infty}^{\infty} \vec{F_{gp_k}} e^{j\left(kt_p\delta - kt_p x\frac{2\pi}{n_p\tau_p}+n_sV\frac{2\pi}{n_p\tau_p}t+\phi\right)} \\ &\quad \times\left(1+2\cos\left(\frac{2\pi}{3}(k-1)\right)\right) \\ &\quad + M_{s0}\frac{\hat{I}}{2}\sum_{k=-\infty}^{\infty} \vec{F_{gp_k}} e^{j\left(kt_p\delta - kt_p x\frac{2\pi}{n_p\tau_p}-n_sV\frac{2\pi}{n_p\tau_p}t-\phi\right)} \\ &\quad \times\left(1+2\cos\left(\frac{2\pi}{3}(k+1)\right)\right) \\ &\quad + \frac{\hat{I}}{2}\sum_{k=-\infty}^{\infty}\sum_{v=-\infty}^{\infty} \vec{F_{gp_k}}\vec{M_{s_v}} \\ &\quad \times e^{j\left(kt_p\delta + n_sv\xi - x\left(kt_p+n_sv\right)\frac{2\pi}{n_p\tau_p}+n_sV\frac{2\pi}{n_p\tau_p}t(1-v)+\phi\right)} \\ &\quad \times\left(1+2\cos\left(\frac{2\pi}{3}(k-1)\right)\right) \end{aligned}$$

TABLE 3. Characteristics of the harmonics of B^m_{gs} and MMF_M.

$B^m_{g_s}$		MMF_M	
Pole Pairs	Travelling Speed	Pole Pairs	Travelling Speed
np_{pm}	0	kt_p	$-\frac{n_sv}{kt_p}$ and $\frac{n_sv}{kt_p}$
$np_{pm}+vn_s$	$\frac{vn_sV}{np_{pm}+vn_s}$	kt_p+n_sv	$-\frac{n_sV(1-v)}{kt_p+n_sv}$ and $\frac{n_sV(1+v)}{kt_p+n_sv}$

$$\begin{aligned} &+ \frac{\hat{I}}{2}\sum_{k=-\infty}^{\infty}\sum_{v=-\infty}^{\infty} \vec{F_{gp_k}}\vec{M_{s_v}} \\ &\quad \times e^{j\left(kt_p\delta + n_sv\xi - x\left(kt_p+n_sv\right)\frac{2\pi}{n_p\tau_p}-n_sV\frac{2\pi}{n_p\tau_p}t(1+v)-\phi\right)} \\ &\quad \left(1+2\cos\left(\frac{2\pi}{3}(k+1)\right)\right). \end{aligned} \tag{57}$$

The airgap flux density that is introduced by the armature into the airgap can now be obtained from

$$B^a_g(x,t) = \frac{\mu_0}{g} MMF_M(x,t). \tag{58}$$

Notice that the armature MMF is also going to create a rich combination of airgap field harmonics. In this case, the 2 latter terms of (57), which appear thanks to the modulation of the secondary rail, are capable of producing static harmonics when $v = 1$. On the other hand the first 2 terms, will only produce dynamic harmonics.

As a summary of the modulation, Table 3 compares the characteristics of the harmonics of B^m_{gs} and MMF_M. Notice that both static and dynamic harmonics exist in both cases. Section V will analyse the linkage of these harmonics, and the thrust force generation mechanism of switched-flux machines.

V. FLUX LINKAGE, BACK-EMF AND THRUST FORCE GENERATION

A. THE FORCE GENERATION PRINCIPLE

In linear electrical machines, the electromagnetic force, F_{em}, can be obtained as the variation of the magnetic energy W_g with respect to the position of the mover x,

$$F_{em} = \frac{dW_g}{dx} = \frac{1}{2}\frac{dL}{dx}I^2 + N_{ph}\frac{d\phi^m_g}{dx}I + \frac{1}{2}\frac{dR_g}{dx}\phi^m_g, \tag{59}$$

where L, ϕ^m_g, R_g, N_{ph} and I are respectively the armature inductance, the flux that is introduced by the magnets in the airgap, the airgap reluctance, the number of turns per phase, and the phase current. The first term of (59) corresponds to the reluctance force component. The second term describes the thrust that is generated due to the interaction between the armature and the PM magnetic fields. The last term is the one that creates the detent-force.

It was identified in [20] that the PM torque is the major contributor in the torque generation of rotating switched-flux machines. In their results, the reluctance torque accounted for about 5 % of the total torque. This is why switched-flux machines are commonly supplied with $i_d = 0$ current. Thus, for the analysis of this article, the machine in Fig. 2 is simulated at pure q axis current. In order to obtain comparable

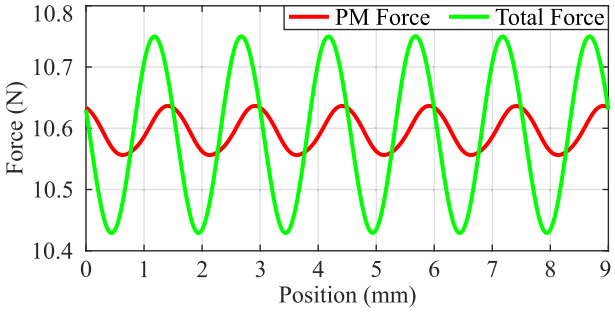

FIGURE 25. PM force vs total force of the example machine.

results to those from a rotating machine, an infinite periodicity was assigned to the simulation model, so that the results were not influenced by the end effect.

The PM force F_{pm} can be calculated from the back-EMF, obtained in an open-circuit simulation, with (60).

$$F_{pm} = \frac{\sum_{n=1}^{m} E_n I_n}{V} \tag{60}$$

The overall force of the example machine, obtained in a pure q axis current FEM simulation, is compared to that which was obtained from the back-EMFs in Fig. 25. The average value of both waveforms is exactly the same. Therefore, the thrust force creation mechanism is explained via the PM force in this section.

B. OPEN CIRCUIT FLUX LINKAGE

In order to obtain the flux linkage of a phase, and therefore, the back-EMF that is generated in a phase winding, the winding function of the phase must be expanded to a Fourier series as

$$F_{ph}(x) = \sum_{k=-\infty}^{\infty} \vec{F_{ph_k}} e^{jkt_p\left(\delta - x\frac{2\pi}{n_p\tau_p}\right)}, \tag{61}$$

where $\vec{F_{ph_k}}$ is the vector of the k-th harmonic and δ is the initial phase of the winding function in radians.

At this point, the open circuit flux linkage Ψ^m_{ph} can be obtained with

$$\Psi^m_{ph}(t) = \int_0^{n_p\tau_p} l_e B^m_{g_p}(x)\, M_s(x,t)\, F_{ph}(x) dx. \tag{62}$$

In order to obtain an average value in the product of two sinusoidal signals, those signals must be of the same frequency. Therefore, only certain combinations of harmonics have the ability to create an average spatial value of flux in the coils of the primary side. The first term in (63) is created by the harmonic combinations that fulfil $np_{pm}+kt_p = 0$, and the second term appears for the combinations where $np_{pm} + kt_p + \nu n_s = 0$.

$$\begin{aligned}\Psi^m_{ph}(t) = l_e n_p \tau_p \times \Bigg[&\sum_{np_{pm}+kt_p=0} M_{s_0} \vec{B^m_{gp_n}} \vec{F_{ph_k}} e^{j(np_{pm}\varphi + kt_p\delta)} \\ &+ \sum_{np_{pm}+kt_p+\nu n_s=0} \vec{M_{s_\nu}} \vec{B^m_{gp_n}} \vec{F_{ph_k}} \\ &\times e^{j\left(np_{pm}\varphi + kt_p\delta + \nu n_s\xi - \nu n_s V\frac{2\pi}{n_p\tau_p}t\right)}\Bigg]\end{aligned} \tag{63}$$

Notice that the first term is just a bias, and is not time dependant. Thus, the harmonic combinations that contribute to the back-EMF are those which fulfil $np_{pm} + kt_p + \nu n_s = 0$.

Another piece of information that can be interpreted from (63) is that the fundamental component of the flux linkage is obtained from the harmonic pairs that are linked through the fundamental component of the secondary modulation function.

It can also be appreciated that the rest of the harmonics of the open circuit flux are obtained with the harmonic pairs that are linked via the higher order harmonics of the modulator. These are commonly very high order harmonics, for example, the 5$^{\text{th}}$ harmonic of the flux is linked via the 65$^{\text{th}}$ airgap harmonic of the modulator. Hence, this harmonic interacts with high order PM field and winding function harmonics. In general, the higher the order of the harmonic, the lower its amplitude will be. This is why well designed switched-flux machines exhibit a very sinusoidal flux-linkage and back-EMF waveform.

C. BACK-EMF

The back-EMF of a phase is the time derivative of the open circuit flux linkage.

$$E^m_{ph}(t) = \frac{d\Psi^m_{ph}(t)}{dt} \tag{64}$$

Substituting (63) in (64) and operating, the expression of the back-EMF yields:

$$\begin{aligned}E^m_{ph}(t) = 2\pi\nu n_s V l_e \sum_{np_{pm}+kt_p+\nu n_s=0} &\vec{M_{s_\nu}} \vec{B^m_{gp_n}} \vec{F_{ph_k}} \\ &\times e^{j\left(np_{pm}\varphi + kt_p\delta + \nu n_s\xi - \nu n_s V\frac{2\pi}{n_p\tau_p}t - \frac{\pi}{2}\right)}\end{aligned} \tag{65}$$

D. THRUST FORCE

For an easier understanding of the result, a formula is calculated for the thrust force that is exerted by each individual phase first. Knowing that,

$$F_{pm_{ph}}(t) = \frac{E_{ph}(t)\, i_{ph}(t)}{V}, \tag{66}$$

that the mechanical linear velocity and the electrical angular speed are related as in

$$\omega = n_s V \frac{2\pi}{n_p \tau_p}, \tag{67}$$

from (65), (51), (53) and (54), and always for $np_{pm} + kt_p + vn_s = 0$, the forces that are generated by the phases can be deduced to be (69), (70) and (71), as shown at the bottom of the page.

The total thrust force of the machine is the sum of the forces that are generated by the individual phases, so by adding (68), (69), and (70), and operating,

$$\begin{aligned} F_{pm}(t) = {} & \pi v n_s V l_e I \left(1 + 2\cos\left(\frac{2\pi}{3}(k-1)\right)\right) \\ & \times \sum_{np_{pm}+kt_p+vn_s=0} \vec{M}_{s_v} \vec{B}^{\vec{m}}_{gp_n} \vec{F}_{ph_k} \\ & \times e^{j\left(\omega t(1-v)+np_{pm}\varphi+kt_p\delta+vn_s\xi-\frac{\pi}{2}+\phi\right)} \\ & + \pi v n_s V l_e I \left(1 + 2\cos\left(\frac{2\pi}{3}(k+1)\right)\right) \\ & \times \sum_{np_{pm}+kt_p+vn_s=0} \vec{M}_{s_v} \vec{B}^{\vec{m}}_{gp_n} \vec{F}_{ph_k} \\ & \times e^{j\left(-\omega t(1+v)+np_{pm}\varphi+kt_p\delta+vn_s\xi-\frac{\pi}{2}-\phi\right)}. \end{aligned} \tag{71}$$

From (71), it can be deduced that the harmonics that create an average value of thrust are the same as those that contribute to the fundamental back-EMF. These will be the harmonic pairs that are linked through $v = 1$ for the first term, and those that are linked through $v = -1$ for the second term. The harmonic pairs that are linked via higher v orders will only produce thrust ripple.

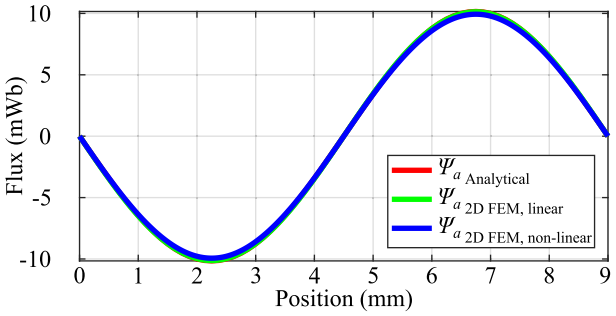

FIGURE 26. Flux linkage of phase a, analytical model vs FEM.

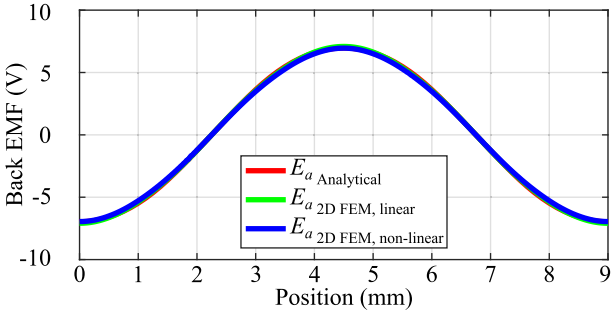

FIGURE 27. Back-EMF of phase a, analytical model vs FEM.

E. COMPARISON OF RESULTS

In this section, the results that were obtained with the analytical expressions are compared to the results of two 2D FEM simulations. The first simulation emulates the model with an ideally permeable material with no saturation, and the second simulation is performed with M800-65A steel. The value of the current has been kept low to avoid excessive saturation.

$$\begin{aligned} F_{pm_a}(t) = {} & \pi v n_s V l_e I \left[\sum_{np_{pm}+kt_p+vn_s=0} \vec{M}_{s_v} \vec{B}^{\vec{m}}_{gp_n} \vec{F}_{ph_k} e^{j\left(\omega t(1-v)+np_{pm}\varphi+kt_p\delta+vn_s\xi-\frac{\pi}{2}+\phi\right)} \right. \\ & \left. + \sum_{np_{pm}+kt_p+vn_s=0} \vec{M}_{s_v} \vec{B}^{\vec{m}}_{gp_n} \vec{F}_{ph_k} e^{j\left(-\omega t(1+v)+np_{pm}\varphi+kt_p\delta+vn_s\xi-\frac{\pi}{2}-\phi\right)} \right], \end{aligned} \tag{68}$$

$$\begin{aligned} F_{pm_b}(t) = {} & \pi v n_s V l_e I \left[\sum_{np_{pm}+kt_p+vn_s=0} \vec{M}_{s_v} \vec{B}^{\vec{m}}_{gp_n} \vec{F}_{ph_k} e^{j\left(\omega t(1-v)+np_{pm}\varphi+kt_p\delta+vn_s\xi-\frac{\pi}{2}+\phi-\frac{2\pi}{3}+k\frac{2\pi}{3}\right)} \right. \\ & \left. + \sum_{np_{pm}+kt_p+vn_s=0} \vec{M}_{s_v} \vec{B}^{\vec{m}}_{gp_n} \vec{F}_{ph_k} e^{j\left(-\omega t(1+v)+np_{pm}\varphi+kt_p\delta+vn_s\xi-\frac{\pi}{2}-\phi+\frac{2\pi}{3}+k\frac{2\pi}{3}\right)} \right], \end{aligned} \tag{69}$$

$$\begin{aligned} F_{pm_c}(t) = {} & \pi v n_s V l_e I \times \left[\sum_{np_{pm}+kt_p+vn_s=0} \vec{M}_{s_v} \vec{B}^{\vec{m}}_{gp_n} \vec{F}_{ph_k} e^{j\left(\omega t(1-v)+np_{pm}\varphi+kt_p\delta+vn_s\xi-\frac{\pi}{2}+\phi+\frac{2\pi}{3}-k\frac{2\pi}{3}\right)} \right. \\ & \left. + \sum_{np_{pm}+kt_p+vn_s=0} \vec{M}_{s_v} \vec{B}^{\vec{m}}_{gp_n} \vec{F}_{ph_k} e^{j\left(-\omega t(1+v)+np_{pm}\varphi+kt_p\delta+vn_s\xi-\frac{\pi}{2}-\phi-\frac{2\pi}{3}-k\frac{2\pi}{3}\right)} \right]. \end{aligned} \tag{70}$$

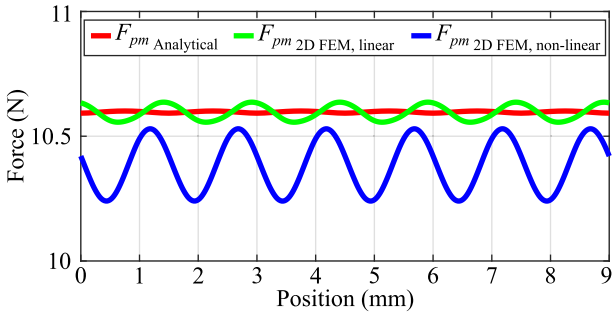

FIGURE 28. PM force, analytical model vs FEM.

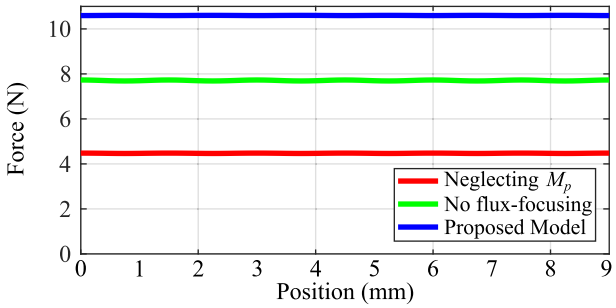

FIGURE 29. Comparison of the different analytical prediction results.

The flux linkage in Fig. 26, the back-EMF (Fig. 27), and the average thrust force in Fig. 28 are very close in all the cases. The fundamental component of the flux linkage, and the back-EMF, and the average thrust force decrease in only 2 % when the non-linear material is used in the simulation. This difference can be appreciated more easily in Fig. 28 due to the scale of the figure.

The prediction of the average thrust force of the analytical model is the same as that of the ideal simulation. When a real material is introduced to the simulation, the output thrust force decreases because the airgap side of the primary teeth gets saturated. Consequently, the airgap flux density lowers, which decreases the average thrust force. This saturation also increases the ripple of the PM thrust force.

In spite of these discrepancies, the model still holds a high enough precision for the analytical sizing of the machine. This is especially true when compared to the models that were previously published in the literature. Fig. 29 compares the thrust force prediction of the proposed model, with the result which would be obtained in the case of a neglected primary modulator or a neglected flux-focusing effect. For the analysed machine, the influence of the primary modulator is so high, that neglecting its influence would lead to imprecise results, as shown in Fig. 29.

VI. DOMINANT THRUST FORCE-GENERATING AIRGAP FIELD HARMONICS AND THEIR INTERACTION

The expressions that were derived in section V-D give a deep insight in the operating mechanism of switched-flux machines. It was concluded that the harmonic combinations that fulfil $np_{pm}+kt_p+vn_s = 0$ and are linked through $v = 1$ or $v = -1$ contribute to the average thrust force. This condition is nonetheless met by an infinite amount of combinations. Wu *et al.* [17] showed that in the reality, only a handful of harmonics are in charge of $> 90\%$ of the force contribution in switched-flux machines. These harmonics are reffered to as the dominant force contributing harmonics in this section.

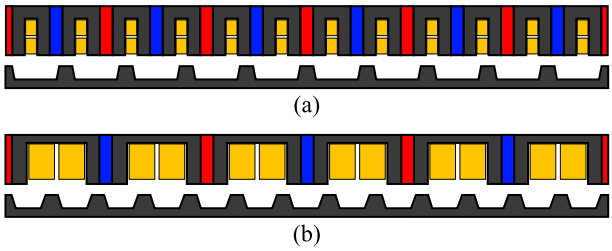

FIGURE 30. (a) U-Core machine and (b) C-Core machine.

TABLE 4. Force contribution of the airgap field harmonics in the U-Core machine.

n	Origin	Order	Contribution (N)	Contribution (%)	$F_{n,\%}$ (%)
1	$\lvert p_{pm} - n_s \rvert$	4	2.58	30.30	84.77
	p_{pm}	6	3.41	39.97	
	$p_{pm} + n_s$	16	1.24	14.5	
3	$\lvert 3p_{pm} - n_s \rvert$	8	-0.98	-11.45	15.60
	$3p_{pm}$	18	1.96	23.04	
	$3p_{pm} + n_s$	28	0.34	4.01	
5	$\lvert 5p_{pm} - n_s \rvert$	20	0.43	0.50	-0.25
	$5p_{pm}$	30	-0.06	-0.76	
	$5p_{pm} + n_s$	40	0.001	0.01	

A. IDENTIFICATION OF THE DOMINANT AIRGAP FIELD HARMONICS

In this section, the dominant force contributing airgap field harmonics are identified for a linear 6/13 C-Core machine and a 12/10 U-Core machine. The machines are shown in Fig. 30. The analysis is done via the Maxwell stress tensor.

The intention of the section is to deliver additional information on the working principle of these machines. The procedure that is explained in this section was taken from [17] and adapted to linear machines.

The analysis starts with an on load time stepping simulation of the machines in 2D FEM. Longitudinal and normal airgap flux density distributions must be obtained in each step of the simulation. Then the waveforms must be expanded to Fourier series, so that the amplitude and the phase of each harmonic are identified.

After this, the force contribution of the k^{th} harmonic, F_k, at the time instant t is obtained with

$$F_k(t) = \frac{l_e n_p \tau_p}{2\mu_0} B_{x_k}(t) B_{y_k}(t) \cos\left(\theta_{y_k}(t) - \theta_{x_k}(t)\right). \quad (72)$$

B_{x_k}, and B_{y_k}, are respectively the amplitude of the longitudinal component of the k^{th} airgap flux density harmonic and its normal component. θ_{x_k} and θ_{y_k} are their respective phase angles.

After computing the force contribution of the harmonics at each of the time steps, the average force that is exerted by each harmonic can be obtained. Table 4 shows the average

TABLE 5. Force contribution of the airgap field harmonics in the C-Core machine.

n	Origin	Order	Contribution (N)	Contribution (%)	$F_{n,\%}$ (%)
1	$\lvert p_{pm} - n_s \rvert$	10	0.60	5.62	12.59
	p_{pm}	3	-0.03	-0.31	
	$p_{pm} + n_s$	16	0.77	7.28	
3	$\lvert 3p_{pm} - n_s \rvert$	4	1.74	16.44	57.02
	$3p_{pm}$	9	3.66	34.53	
	$3p_{pm} + n_s$	22	0.641	6.05	
5	$\lvert 5p_{pm} - n_s \rvert$	2	-0.47	-4.44	29.51
	$5p_{pm}$	15	3.47	32.79	
	$5p_{pm} + n_s$	28	0.12	1.16	

thrust force contribution of 9 airgap harmonics of the U-Core machine, and the same data is given for the C-Core machine in Table 5. Thanks to (71), it is possible to identify the origin of the harmonic from $np_{pm} + kt_p + vn_s = 0$. n is the harmonic order of the equivalent airgap flux density accounting for the primary modulator, (46).

From tables 4 and 5 it can be observed that both the static and the dynamic airgap field harmonics generate thrust force. This might seem counter-intuitive in the first place, especially when taking into account that only the dynamic airgap field harmonics contribute to the back-EMF of the machine. On the other hand, it was analysed from (63) that only those harmonics that are linked through the fundamental component of the secondary modulator contribute to the thrust force.

B. THE INTERACTION BETWEEN THE STATIC AND DYNAMIC HARMONICS

To analyse the issue, take the airgap harmonic of order 4 of the C-Core machine (in Table 5) as an example. This is a dynamic harmonic that originates from $\lvert 3p_{pm} - n_s \rvert$. Hence, its displacement is the result of the modulation of the secondary rail to the field of the PMs. This harmonic order can originate from the combination of either $n = 3$ and $v = -1$ or the combination of $n = -3$ and $v = 1$. If we consider that in order for that harmonic to be linked by the armature, the condition

$$np_{pm} + kt_p + vn_s = 0 \tag{73}$$

must be met, we can obtain the order of the armature MMF harmonic that interacts with the aforementioned combination from

$$3p_{pm} - n_s = -kt_p \rightarrow k = 2 \quad \text{for } n = 3 \text{ and } v = -1, \text{ and} \tag{74}$$

$$-3p_{pm} + n_s = -kt_p \rightarrow k = -2 \quad \text{for } n = -3 \text{ and } v = 1. \tag{75}$$

Bringing back the expression of the modulated armature MMF,

$$\begin{aligned} &MMF_M(x,t) \\ &= M_{s_0}\frac{\hat{I}}{2}\sum_{k=-\infty}^{\infty}\vec{F_{gp_k}}e^{j\left(kt_p\delta - kt_p x\frac{2\pi}{np\tau_p} + n_s V\frac{2\pi}{np\tau_p}t + \phi\right)} \\ &\quad\times\left(1 + 2\cos\left(\frac{2\pi}{3}(k-1)\right)\right) \\ &\quad + M_{s_0}\frac{\hat{I}}{2}\sum_{k=-\infty}^{\infty}\vec{F_{gp_k}}e^{j\left(kt_p\delta - kt_p x\frac{2\pi}{np\tau_p} - n_s V\frac{2\pi}{np\tau_p}t - \phi\right)} \\ &\quad\times\left(1 + 2\cos\left(\frac{2\pi}{3}(k+1)\right)\right) \\ &\quad + \frac{\hat{I}}{2}\sum_{k=-\infty}^{\infty}\sum_{v=-\infty}^{\infty}\vec{F_{gp_k}}\vec{M_{s_v}} \\ &\quad\times e^{j\left(kt_p\delta + n_s v\xi - x\left(kt_p + n_s v\right)\frac{2\pi}{np\tau_p} + n_s V\frac{2\pi}{np\tau_p}t(1-v) + \phi\right)} \\ &\quad\times\left(1 + 2\cos\left(\frac{2\pi}{3}(k-1)\right)\right) \\ &\quad + \frac{\hat{I}}{2}\sum_{k=-\infty}^{\infty}\sum_{v=-\infty}^{\infty}\vec{F_{gp_k}}\vec{M_{s_v}} \\ &\quad\times e^{j\left(kt_p\delta + n_s v\xi - x\left(kt_p + n_s v\right)\frac{2\pi}{np\tau_p} - n_s V\frac{2\pi}{np\tau_p}t(1+v) - \phi\right)} \\ &\quad\times\left(1 + 2\cos\left(\frac{2\pi}{3}(k+1)\right)\right), \end{aligned} \tag{76}$$

and taking into account that $\left(1 + 2\cos\left(\frac{2\pi}{3}(k-1)\right)\right) = 0$ for $k = 2$, and $\left(1 + 2\cos\left(\frac{2\pi}{3}(k+1)\right)\right) = 0$ for $k = -2$,

$$\begin{aligned} &MMF_{M_2}(x,t) \\ &= M_{s_0}\frac{3\hat{I}}{2}\vec{F_{gp_2}}e^{j\left(2t_p\delta - 2t_p x\frac{2\pi}{np\tau_p} - n_s V\frac{2\pi}{np\tau_p}t - \phi\right)} \\ &\quad + \frac{3\hat{I}}{2}\sum_{v=-\infty}^{\infty}\vec{F_{gp_2}}\vec{M_{s_v}} \\ &\quad\times e^{j\left(2t_p\delta + n_s v\xi - x\left(2t_p + n_s v\right)\frac{2\pi}{np\tau_p} - n_s V\frac{2\pi}{np\tau_p}t(1+v) - \phi\right)}, \end{aligned} \tag{77}$$

and

$$\begin{aligned} &MMF_{M_{-2}}(x,t) \\ &= M_{s_0}\frac{3\hat{I}}{2}\vec{F_{gp_{-2}}}e^{j\left(-2t_p\delta + 2t_p x\frac{2\pi}{np\tau_p} + n_s V\frac{2\pi}{np\tau_p}t + \phi\right)} \\ &\quad + \frac{3\hat{I}}{2}\sum_{v=-\infty}^{\infty}\vec{F_{gp_{-2}}}\vec{M_{s_v}} \\ &\quad\times e^{j\left(-2t_p\delta + n_s v\xi - x\left(-2t_p + n_s v\right)\frac{2\pi}{np\tau_p} + n_s V\frac{2\pi}{np\tau_p}t(1-v) + \phi\right)}. \end{aligned} \tag{78}$$

Replacing v with its corresponding value for each MMF harmonic,

$$\begin{aligned} &MMF_{M_2}(x,t) \\ &= M_{s_0}\frac{3\hat{I}}{2}\vec{F_{gp_2}}e^{j\left(2t_p\delta - 2t_p x\frac{2\pi}{np\tau_p} - n_s V\frac{2\pi}{np\tau_p}t - \phi\right)} \\ &\quad + \frac{3\hat{I}}{2}\vec{F_{gp_2}}\vec{M_{s_{-1}}}e^{j\left(2t_p\delta - n_s\xi - x\left(2t_p - n_s\right)\frac{2\pi}{np\tau_p} - \phi\right)}, \end{aligned} \tag{79}$$

and

$$\begin{aligned} &MMF_{M_{-2}}(x,t) \\ &= M_{s_0}\frac{3\hat{I}}{2}\vec{F_{gp_{-2}}}e^{j\left(-2t_p\delta + 2t_p x\frac{2\pi}{np\tau_p} + n_s V\frac{2\pi}{np\tau_p}t + \phi\right)} \\ &\quad + \frac{3\hat{I}}{2}\vec{F_{gp_{-2}}}\vec{M_{s_1}}e^{j\left(-2t_p\delta + n_s\xi - x\left(-2t_p + n_s\right)\frac{2\pi}{np\tau_p} + \phi\right)}. \end{aligned} \tag{80}$$

Now, remembering that only the MMF harmonics that are modulated by the fundamental component of M_s contribute to the thrust force, observe that the airgap harmonics that are obtained from $k = 2$ and $v = -1$ in (79) and from $k = -2$ and $v = 1$ in (80), are actually static. Moreover, the equivalent airgap field harmonic orders that are obtained after the modulation are -9 and 9. Remember that the procedure started with the analysis of the airgap field harmonics of orders 4 and -4, which are dynamic, and now we ended up with orders 9 and -9, with these last two being static. The phenomenon is not specific to this combination of harmonics, and can be replicated with any harmonic order from Table 5. The same thing still happens in the case of the U-Core machine, but the arrangement of the winding is different, and the expressions of the force and the MMF must be obtained again, with

$$kt_p\delta_a = kt_p\delta \quad kt_p\delta_b = kt_p\left(\delta - \frac{2\pi}{3t_p}\right) \quad kt_p\delta_c = kt_p\left(\delta + \frac{2\pi}{3t_p}\right). \tag{81}$$

Also notice that the modulation of the PM field produces a harmonic order that can be perceived by the armature, and that the modulation of the armature field produces a harmonic order that can be linked by the static PM MMF. This is actually the function of the modulator in switched-flux machines. It acts as an interface between airgap field harmonics of different orders, allowing the linkage of the PM and the armature fields.

In some aspects, switched-flux PM machines are similar to conventional PM machines. In a conventional surface PM machine, from the point of view of the rotor PMs, the magnetic field that is introduced by the armature is perceived as static, because it is synchronous to the rotation speed of the rotor. On the other hand, the static armature perceives a rotating magnetic field from the magnets, which creates back-EMF in the windings. The same principle applies to switched-flux machines. The PMs must perceive a magnetic field that is synchronous to them, or in a single word, static. On the other hand, the armature winding has to perceive an alternating magnetic field in order to create back-EMF, and hence, only after the interaction of the PM field harmonics with the secondary rail is it possible to obtain a back-EMF.

Consequently, it does make sense for both the static and the dynamic harmonics to produce force in switched-flux machines. They are linked with each other via the modulator, and it is their interaction which produces thrust force. As for the back-EMF, we mentioned that only the dynamic harmonics can produce a flux derivative in the phase coils. This is true, because the static harmonics cannot produce any back-EMF by themselves. However, the dynamic open-circuit filed harmonics are the manifestation of the static harmonics that are introduced by the PMs, after being modulated by the secondary poles. Hence, although indirectly, it is the static PM MMF harmonics which produce back-EMF.

TABLE 6. PM field harmonic efficiency ratio of the U-Core and C-Core machines.

	U-Core			C-Core		
n	1	3	5	1	3	5
$F_{n,\%}$ (%)	84.77	15.6	-0.25	12.59	57.02	29.51
$\hat{B}^m_{gp_n}$ (T)	0.38	0.22	0.02	0.21	0.25	0.14
η_{F_n} (%/T)	225.2	71.0	-13.2	58.8	230.6	211.2

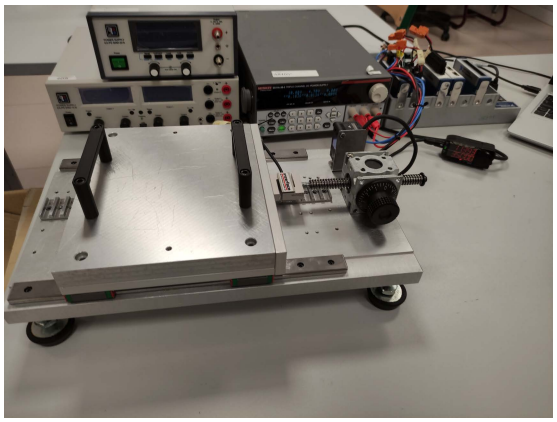

FIGURE 31. Test bench.

C. THE EFFICIENCY OF PM FIELD HARMONICS

If the analysis is taken one step further, an interesting difference can be identified between Table 4 and Table 5. Notice that the harmonics that originate in the p_{pm} pole pair harmonic of the PM field (orders 4, 6, and 16) produce 84.77 % of the final thrust force of the U-Core machine. In this aspect, the U-Core switched-flux machine is very similar to the conventional surface PM machines. In both of these machine types, it is mainly the fundamental PM harmonic which is in charge of creating the average thrust force.

However, in the case of the C-Core machine, it is the 3$^{\text{rd}}$ and the 5$^{\text{th}}$ PM field harmonics, with 57.02 % and 29.51% contribution respectively, which combine for the 86.53 % of the total force contribution.

Notice that for the C-Core machine, the amplitude of the fundamental PM field harmonic in Table 6 is very similar to that of the 3$^{\text{rd}}$ harmonic. Despite this, the airgap field harmonics that originate in the fundamental component only add up to 12.59 % in the contribution of the average thrust force. Therefore, if the PM field harmonic efficiency ratio, η_{F_n}, is defined as

$$\eta_{F_n} = \frac{F_{n,\%}}{\hat{B}^m_{gp_n}}, \tag{82}$$

where $F_{n,\%}$ is the percentage contribution of the n^{th} PM field harmonic to the average thrust force, and $\hat{B}^m_{gp_n}$ is the amplitude of the n^{th} PM field harmonic, the most efficient PM field harmonics can be identified. Table 6 shows the PM field harmonic efficiency ratios of the most dominant PM field harmonics of the analysed machines.

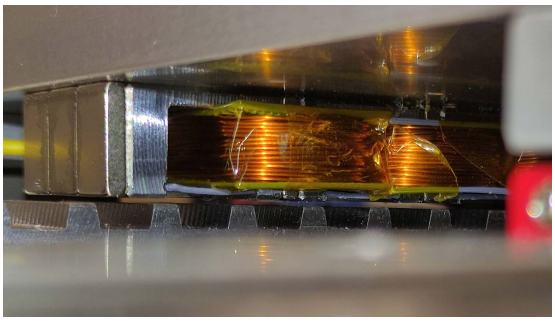

FIGURE 32. Closeup of the LSFPM prototype.

TABLE 7. Main parameters of the prototype.

Parameter	Symbol	Unit	Value
Active Length	l_a	mm	144
Machine Depth	l_{stk}	mm	30
Total Height	h_t	mm	21
Airgap	g	mm	1
Primary Slot Width	ω_{ps}	mm	12.8
Secondary Slot Width	ω_{ss}	mm	8
PM Width	ω_{pm}	mm	3
PM Height	h_{pm}	mm	14.4
Turns per Phase	N_{ph}	Turns	234
PM Remanence	B_r	T	1.17
PM Relative Permeability	μ_r		1.06

It can be concluded from Table 6 that not only are the fundamental PM field harmonic for the U-Core machine, and the 3rd and 5th harmonics in the C-Core machine the most dominant harmonics, but they are also the most efficient.

Now observe the influence of the primary slots in the spectra of Fig. 12 and Fig. 13. The fundamental harmonic's amplitude is lowered when the machine is slotted, whereas that of the 3rd and 5th harmonics is increased. This means that the distortion that is introduced by the primary slots is a parasitic effect for the conventional U-Core machines, but, it is actually beneficial for C-Core machines. Therefore, it can be stated that on the one hand, U-Core machines could benefit from the usage of semi-closed slots, which minimise the distortion of the primary slots. On the other hand, the C-Core machines are best fitted for open-slot configurations.

VII. EXPERIMENTAL VALIDATION

The experimental validation of the model was carried out via a linear C-Core switched-flux machine prototype. The static force of the machine was measured in the test bench from Fig. 31. The prototype is shown in Fig. 32, and its main parameters are given in Table 7.

In general, the phase back-EMF amplitude is unbalanced in linear machines. This is caused by the end effect. Additionally, the end-effect generates a thrust ripple component. Thus, the prototype has additional poles attached in its ends to help to reduce the thrust ripple and the back-EMF unbalance [27]. In this way, it can be assumed that the average thrust force of the machine will be fairly close to the one that would be obtained with an ideally periodical machine.

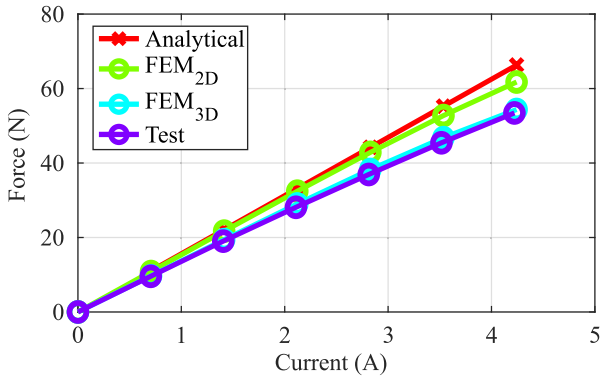

FIGURE 33. Comparison of results.

A comparison between the experimental results, 2D and 3D FEM predictions, and the analytical model is given in Fig. 33. Notice in Table 7 that the stacking length of the prototype is small. Hence, the influence of the transverse flux leakage is quite severe for the prototype. This is why the experimental results and the results from the 3D FEM simulations differ from the predictions from the 2D simulations and the analytical model in Fig. 33.

As the simulations were solved with non-linear materials, the error of the analytical model increases when high current values are used. Even so, the maximal error of the analytical model when compared to the 2D simulation was of 6.8 % at maximum current. Hence, it can be concluded that the model is capable to give a highly accurate prediction of the performance of switched-flux machines, especially at low saturation values.

VIII. CONCLUSION

In this article, an analytical tool was presented for the prediction and analysis of the electromagnetic performance of switched-flux PM machines. The model was validated with 2D and 3D FEM simulations and experimental measurements to a linear SFPM prototype. It was demonstrated that the model can predict the performance of switched-flux machines with high accuracy, even when the machine that is being analysed has a wide slot opening, which was not possible from the previous publications from the literature as it was demonstrated in Fig. 29.

The hybrid MMF-permeance and MEC model was used first to describe the operating mechanism of switched-flux machines. It was observed how the flux focusing effect is a crucial part of the operation of certain switched-flux machines with large slot openings. The analytical expressions also explained the sinusoidal nature of the back-EMF waveforms and the linkage between the armature and PM field harmonics.

Thanks to the MMF-permeance model, the origin of the dominant airgap field harmonics was explained, and the most efficient PM field harmonics were identified. This efficiency was used to highlight that semi-closed slots can improve the performance of the U-Core machine, whilst they can be

detrimental for the C-Core configuration, more suited for open slots.

The model was developed assuming a ferromagnetic material with an infinite permeability, and an infinitely long periodic machine. Therefore, the saturation effect, and the influence of the end effect are ignored by the analytical predictions. Despite this, the prediction of the PM force showed a good agreement when compared to the simulations and the experimental results.

Further developments of the model could include the implementation of the saturation effect in the model. In this aspect, a nonlinear equivalent magnetic circuit was used in [28] to analyse a linear switched-flux machine. A similar approach would yield highly precise results when combined with the proposed model. The implementation of the improved conformal transformation [23], could also be used to enhance the precision of the analytical tool. Moreover, an additional relative permeance component could also be implemented to account for the end effect, and predict the waveform of the detent force. Another alternative would be to obtain the on-load magnetic field distribution from a subdomain model. This kind of model has already been used successfully for the prediction of the performance of switched-flux machines in [29].

The upcoming works of the authors will be focused on further developments of the analytical model, and the optimisation of the performance of linear switched-flux machines.

REFERENCES

[1] R. Cao, M. Lu, N. Jiang, and M. Cheng, "Comparison between linear induction motor and linear flux-switching permanent-magnet motor for railway transportation," *IEEE Trans. Ind. Electron.*, vol. 66, no. 12, pp. 9394–9405, Dec. 2019.

[2] A. S. Thomas, Z. Q. Zhu, R. L. Owen, G. W. Jewell, and D. Howe, "Multi-phase flux-switching permanent-magnet brushless machine for aerospace application," *IEEE Trans. Ind. Appl.*, vol. 45, no. 6, pp. 1971–1981, Nov./Dec. 2009.

[3] R. Cao, C. Mi, and M. Cheng, "Quantitative comparison of flux-switching permanent-magnet motors with interior permanent magnet motor for EV, HEV, and PHEV applications," *IEEE Trans. Magn.*, vol. 48, no. 8, pp. 2374–2384, Aug. 2012.

[4] H. Ding, W. Sixel, L. Zhang, A. Hembel, L. Handy-Cardenas, G. Nellis, and B. Sarlioglu, "Evaluation of the self-cooling performance of a flux-switching permanent magnet machine with airfoil-shaped rotor," *IEEE Trans. Ind. Appl.*, vol. 57, no. 4, pp. 3710–3721, Jul. 2021.

[5] I. Eguren, G. Almandoz, A. Egea, G. Ugalde, and A. J. Escalada, "Linear machines for long stroke applications—A review," *IEEE Access*, vol. 8, pp. 3960–3979, 2020.

[6] B. Zhang, M. Cheng, S. Zhu, M. Zhang, W. Hua, and R. Cao, "Investigation of linear flux-switching permanent magnet machine for ropeless elevator," in *Proc. 19th Int. Conf. Electr. Mach. Syst. (ICEMS)*, Chiba, Japan, Nov. 2016, pp. 1–5.

[7] L. Huang, H. Yu, M. Hu, J. Zhao, and Z. Cheng, "A novel flux-switching permanent-magnet linear generator for wave energy extraction application," *IEEE Trans. Magn.*, vol. 47, no. 5, pp. 1034–1037, May 2011.

[8] R. Cao, Y. Jin, Z. Zhang, and M. Cheng, "A new double-sided linear flux-switching permanent magnet motor with yokeless mover for electromagnetic launch system," *IEEE Trans. Energy Convers.*, vol. 34, no. 2, pp. 680–690, Jun. 2019.

[9] W. Hao and Y. Wang, "Analysis of double-sided sandwiched linear flux-switching permanent-magnet machines with staggered stator teeth for urban rail transit," *IET Elect. Syst. Transp.*, vol. 8, no. 3, pp. 175–181, Sep. 2018.

[10] R. Cao, M. Cheng, C. Mi, W. Hua, X. Wang, and W. Zhao, "Modeling of a complementary and modular linear flux-switching permanent magnet motor for urban rail transit applications," *IEEE Trans. Energy Convers.*, vol. 27, no. 2, pp. 489–497, Jun. 2012.

[11] R. Cao, M. Cheng, and W. Hua, "Investigation and general design principle of a new series of complementary and modular linear FSPM motors," *IEEE Trans. Ind. Electron.*, vol. 60, no. 12, pp. 5436–5446, Dec. 2013.

[12] R. Cao, M. Cheng, C. C. Mi, and W. Hua, "Influence of leading design parameters on the force performance of a complementary and modular linear flux-switching permanent-magnet motor," *IEEE Trans. Ind. Electron.*, vol. 61, no. 5, pp. 2165–2175, May 2014.

[13] Z. Q. Zhu and J. T. Chen, "Advanced flux-switching permanent magnet brushless machines," *IEEE Trans. Magn.*, vol. 46, no. 6, pp. 1447–1453, Jun. 2010.

[14] Z. Q. Zhu, J. T. Chen, Y. Pang, D. Howe, S. Iwasaki, and R. Deodhar, "Analysis of a novel multi-tooth flux-switching PM brushless AC machine for high torque direct-drive applications," *IEEE Trans. Magn.*, vol. 44, no. 11, pp. 4313–4316, Nov. 2008.

[15] J. T. Chen, Z. Q. Zhu, and D. Howe, "Stator and rotor pole combinations for multi-tooth flux-switching permanent-magnet brushless AC machines," *IEEE Trans. Magn.*, vol. 44, no. 12, pp. 4659–4667, Dec. 2008.

[16] W. Min, J. T. Chen, Z. Q. Zhu, Y. Zhu, M. Zhang, and G. H. Duan, "Optimization and comparison of novel E-core and C-core linear switched flux PM machines," *IEEE Trans. Mag.*, vol. 47, no. 8, pp. 2134–2141, Aug. 2011.

[17] Z. Z. Wu and Z. Q. Zhu, "Analysis of air-gap field modulation and magnetic gearing effects in switched flux permanent magnet machines," *IEEE Trans. Magn.*, vol. 51, no. 5, pp. 1–12, May 2015.

[18] Z. Zeng, Y. Shen, Q. Lu, D. Gerada, B. Wu, X. Huang, and C. Gerada, "Flux-density harmonics analysis of switched-flux permanent magnet machines," *IEEE Trans. Magn.*, vol. 55, no. 6, pp. 1–7, Jun. 2019.

[19] P. Wang, W. Hua, G. Zhang, B. Wang, and M. Cheng, "Principle of flux-switching permanent magnet machine by magnetic field modulation theory—Part I: Back-electromotive-force generation," *IEEE Trans. Ind. Electron.*, vol. 69, no. 3, pp. 2370–2379, Mar. 2022.

[20] P. Wang, W. Hua, G. Zhang, B. Wang, and M. Cheng, "Principle of flux-switching PM machine by magnetic field modulation theory—Part II: Electromagnetic torque generation," *IEEE Trans. Ind. Electron.*, vol. 69, no. 3, pp. 2437–2446, Mar. 2022.

[21] M. Cheng, P. Han, and W. Hua, "General airgap field modulation theory for electrical machines," *IEEE Trans. Ind. Electron.*, vol. 64, no. 8, pp. 6063–6074, Aug. 2017.

[22] Z. Q. Zhu and D. Howe, "Instantaneous magnetic field distribution in brushless permanent magnet DC motors. III. Effect of stator slotting," *IEEE Trans. Magn.*, vol. 29, no. 1, pp. 143–151, Jan. 1993.

[23] F. R. Alam and K. Abbaszadeh, "Magnetic field analysis in eccentric surface-mounted permanent-magnet motors using an improved conformal mapping method," *IEEE Trans. Energy Convers.*, vol. 31, no. 1, pp. 333–344, Mar. 2016.

[24] H. Chen, R. Nie, and W. Zhao, "A novel tubular switched reluctance linear launcher with a module stator," *IEEE Trans. Plasma Sci.*, vol. 47, no. 5, pp. 2539–2544, May 2019.

[25] H. Chen, A. M. EL-Refaie, and N. A. O. Demerdash, "Flux-switching permanent magnet machines: A review of opportunities and challenges—Part II: Design aspects, control, and emerging trends," *IEEE Trans. Energy Convers.*, vol. 35, no. 2, pp. 699–713, Jun. 2020.

[26] T. Lipo, *Analysis of Synchronous Machines*, 2nd ed. Boca Raton, FL, USA: CRC Press, 2012.

[27] I. Eguren, G. Almandoz, A. Egea, S. Zarate, and A. Urdangarin, "End magnet optimisation for the reduction of the thrust ripple of linear switched-flux machines," in *Proc. Int. Conf. Electr. Mach. (ICEM)*, Aug. 2020, pp. 700–706.

[28] S. Zhou, H. Yu, M. Hu, C. Jiang, and L. Huang, "Nonlinear equivalent magnetic circuit analysis for linear flux-switching permanent magnet machines," *IEEE Trans. Magn.*, vol. 48, no. 2, pp. 883–886, Feb. 2012.

[29] X. Wu and Y. Zhou, "Analytical calculation of electromagnetic performances of bearingless flux-switching permanent-magnet machine considering iron saturation based on exact subdomain model," *IEEE Access*, vol. 7, pp. 158858–158871, 2019.

IMANOL EGUREN was born in Anoeta, Basque Country, Spain, in 1993. He received the B.S. degree in electronics engineering from Mondragon Unibertsitatea, Mondragón, Spain, in 2015, where he is currently pursuing the Ph.D. degree.

His current research interest includes design, control, and optimization of linear machines.

GAIZKA ALMANDOZ (Member, IEEE) was born in Arantza, Spain. He received the B.Sc. and Ph.D. degrees in electrical engineering from Mondragon Unibertsitatea, Mondragón, Spain, in 2003 and 2008, respectively.

Since 2003, he has been with the Department of Electronics and Computing, Faculty of Engineering, Mondragon Unibertsitatea, where he is currently an Associate Professor. His current research interest includes design, modeling, and control of electrical machine. He has participated in various research projects in the fields of wind energy systems, elevator drive, and railway traction.

ARITZ EGEA received the degree in electrical engineering from the University of Mondragon, Mondragon, Spain, in 2009, and the Ph.D. degree in electrical engineering in 2012.

He is currently an Associate Professor with the Faculty of Engineering, Mondragon Unibertsitatea. His current research interests include electrical machine design and control and electromagnetic actuators.

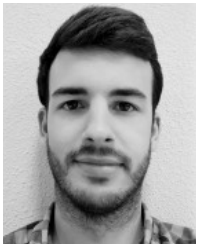

XABIER BADIOLA received the B.Eng. degree in electronic engineering and the Ph.D. degree in applied engineering from Mondragon Unibertsitatea, Mondragón, Spain, in 2013 and 2019, respectively.

Since 2019, he has been with the Department of Electronics, Faculty of Engineering, Mondragon Unibertsitatea, where he is currently an Associate Professor. His current research interests include the control and modeling of electrical machines for automotive applications.

ANDER URDANGARIN was born in Ordizia, Spain, in February 1982. He received the B.S. degree in automatic and industrial electronics from Mondragon Unibertsitatea, Mondragón, Spain, in 2009.

From 2010 to 2012, he was with the Department of Electronics, Faculty of Engineering, Mondragon Unibertsitatea. Since 2012, he has been a member of ORONA. His current research interests include power electronics design, modeling, and control.